# Numerical sensitivity assessment of key factors influencing residual stress distributions in wire arc additively manufactured components

***Xiongfeng Ruan*** [1, 2, *]***, Barbara Rossi*** [1, 2]

[1] *KU Leuven, Faculty of Engineering Technology, Sint-Katelijne-Waver, Belgium.*

[2] *University of Oxford, Department of Engineering Science, Oxford, United Kingdom.*

*Corresponding author

Email address: xiongfeng.ruan@kuleuven.be, xiongfeng.ruan@eng.ox.ac.uk

## Abstract

This study investigates temperature evolution, stress development, residual stress distribution, and deformation in carbon steel components manufactured via cold metal transfer (CMT)-based wire arc additive manufacturing (WAAM) using 3Dprint AM35 wire feed (S355 grade). Three-dimensional coupled thermal-mechanical finite element (FE) models were developed and validated using experimental measurements, including FLIR thermography, thermocouples, strain gauges, and 3D laser scanning. Parametric analyses of the deposition layers and platform concepts on the thermal behaviour and residual stress distributions are evaluated through additional case studies. Additionally, a detailed sensitivity analysis investigates the influence of key FE simulation parameters, including analysis techniques, surface convection and radiation coefficients, heat source parameters, and bolt pretension forces. For specimens with different deposition layers, the transverse residual stresses exhibit a zigzag pattern of alternating tension and compression along the deposition height. Meanwhile, the results also indicate that the sequentially coupled thermal-stress analysis enables faster computation but underestimates temperature values and is less accurate in predicting residual stress distributions. It was also observed that the residual stresses are highly sensitive to boundary conditions, which can be partly removed by removing the substrate. The findings provide valuable guidance for developing reliable FE models and deepening the understanding of thermo-mechanical behaviour in additively manufactured structures. This supports more accurate prediction and control of residual stress patterns under varying process conditions, ultimately guaranteeing the design reliability of load-bearing WAAM components.

## Keywords

Wire-arc additive manufacturing; Finite element modelling; Residual stress; Sensitivity analysis.

# 1 Introduction

Robotic additive manufacturing, particularly using gas metal arc welding, has gained significant traction in recent years due to its high deposition rates and ease of implementation [1–3]. In this process, each sequence deposits a single layer of material following a predefined geometry, with multiple passes combined to create a three-dimensional workpiece. Wire-arc additive manufacturing (WAAM) offers many advantages, including low capital investment using off-the-shelf equipment, high energy efficiency (approximately 90%), and deposition rates ranging from 0.5 to 10 kg/h making it highly efficient and productive [4–6], establishing WAAM as one of the most widely used additive manufacturing technologies.

Research on WAAM for metal part production has expanded rapidly since 2013, with related publications representing 17.8% of all additive manufacturing research papers [7–9]. Research on WAAM covers a wide range of topics. For instance, Huang et al. [10] examined the stress-strain behaviour of WAAM specimens fabricated using different feedstock wires, surface conditions, material thicknesses, loading directions and printing strategies. They developed constitutive models capable of accurately predicting the full stress-strain curves of WAAM steels, making them suitable for integration into analytical, numerical, and design models for WAAM steel structures. Additionally, Huang et al. [11] explored the mechanical properties of WAAM steel plates at polar temperatures. Their findings revealed that Young's modulus, strength, and ductility increased as the temperature decreased, with the most pronounced improvement observed in the ultimate tensile strength. Moreover, finite element (FE) thermo-mechanical numerical simulations have proven to be valuable for understanding the fundamental mechanisms occurring during the WAAM process [12–15]. Interest in this field has grown significantly since 2016 [16], driven by advancements in commercial simulation software and computational capabilities, including ANSYS [17], ABAQUS [18], COMSOL [19], FLOW-3D [20], and in-house codes [21]. Numerical studies on WAAM encompass a wide range of scales and physical phenomena. At the component's scale, models primarily focus on calculating thermal cycles, residual stress and deformations [22–27]. At the

mesoscale, research mostly examines molten pool dynamics, while multi-scale models investigate microstructure evolution and the mechanical properties [19,21,28–30].

For engineering structures, understanding the thermal development, stress evolution, deformation, and residual stress distribution during the WAAM process is crucial, as these factors significantly impact structural performance and service reliability [10,31]. To study these phenomena, macroscale models that simulate the heat transfer and mechanical behaviour are widely used [32,33]. For example, Li et al. [25] developed a transient three-dimensional FE model to simulate thermal stress evolution and residual stress distribution in circular thin-walled structures. Li et al. [26] employed FE models to analyse the effects of deposition path on residual stress and distortion in laser and cold metal transfer hybrid additive manufacturing. Montevecchi et al. [34] introduced a novel heat source model that accounts for the actual power distribution between the filler and base metals. In [27], Dong et al. developed a modified inherent strain method to predict residual stress and distortion in Ti6Al4V components, achieving high simulation accuracy with a computational time 13 times less than detailed process simulations.

Residual stress patterns in WAAM components have been widely studied [23–27,35–39], providing valuable insights into their distributions and influencing factors. Sun et al. [35] analysed residual stress in aluminium components with varying deposition layers and concluded that stress patterns are strongly affected by the number of layers. Wu et al. [36] examined process parameters influencing residual stress distribution and identified substrate preheat temperature as the most significant factor as residual stresses originate during cooling. Huang et al. [37] investigated residual stress in wall and pipe structures made from 308LSi feedstock. They observed a distinct longitudinal (or circumferential) residual stress pattern: tensile stresses near the top surface, compressive stresses close to the substrate surface, and tensile stresses reappearing near the bottom of the substrate. Similarly, Yuan et al. [38] reported that WAAM specimens, regardless of material, printed method, or dimensions, consistently exhibit similar zig-zag type residual stress patterns along height. Kyvelou et al. [40] investigated hot-rolled steel I-sections reinforced with WAAM-fabricated stiffeners added to the flange tips. The study took advantage of residual stresses by prestressing the flange tips of

steel sections against subsequent compressive loading, thereby delaying yielding and increasing the load-bearing capacity.

Although FE modelling has been used to analyse residual stress distributions in WAAM components, systematic studies investigating the effects of component geometries, boundary conditions and modelling parameters on residual stresses are still lacking. The sensitivity of residual stresses to various numerical simulation parameters is not yet fully understood due to the complexity of multi-scale interactions and coupled physical phenomena. Different studies use different heat loss parameters (surface convection and radiation coefficients) [22,41,42] resulting in inconsistent simulated thermal cycles and residual stress distributions. This study develops and validates a FE model to systematically analyse residual stresses in components produced using cold metal transfer based WAAM. Using 3Dprint AM35, an unalloyed carbon steel equivalent to S355 grade, this research goes beyond conventional sensitivity studies by investigating the sensitivity of numerical simulations to modelling parameters such as modelling method, heat loss parameters, heat input, and bolt pretension that significantly influence residual stress evolution. Through a detailed case study, this work aims to establish a more accurate and more reliable modelling framework, providing deeper and more general insights into residual stress behaviour and guiding process optimization.

The structure of this paper is organised as follows: Section 2 describes the WAAM experimental process, including the preparation of specimens and the measurement of the temperature field, strain and profile distortion. Section 3 provides details on the FE modelling process, covering the governing equations, heat source model, and computational settings. Section 4 presents the validation of the FE results against experimental measurements. Section 5 conducts a case study to analyse the residual stress distribution within the specimens under varying layer deposition scenarios and boundary conditions. Section 6 examines the sensitivity of the numerical results to key modelling parameters. Finally, Section 7 summarises the conclusions of this study.

## 2 Experiments

### 2.1 Experimental setup

The cold metal transfer (CMT)-based WAAM process was used for material deposition due to its advantages in precisely controlling heat input and deposition rate, achieved through high-speed digital control and an advanced wire feeding system [8]. A Fronius TPS600i power source was used as the heat source, which was installed on a 6-axis KR16 R2010 KUKA robot to ensure precise movement during deposition. The solid wire used for deposition was the 3Dprint AM35 series from the supplier Voestalpine Böhler Welding. AM35 corresponds to deposition material of unalloyed carbon steel S355. The wire, with a diameter of 1.2 mm, was melted and deposited onto a substrate to deposit flat specimens. The chemical compositions and mechanical properties of both the wire feed and substrate are summarized in Table 1 and Table 2 respectively. The experimental setup is schematically illustrated in Fig. 1.

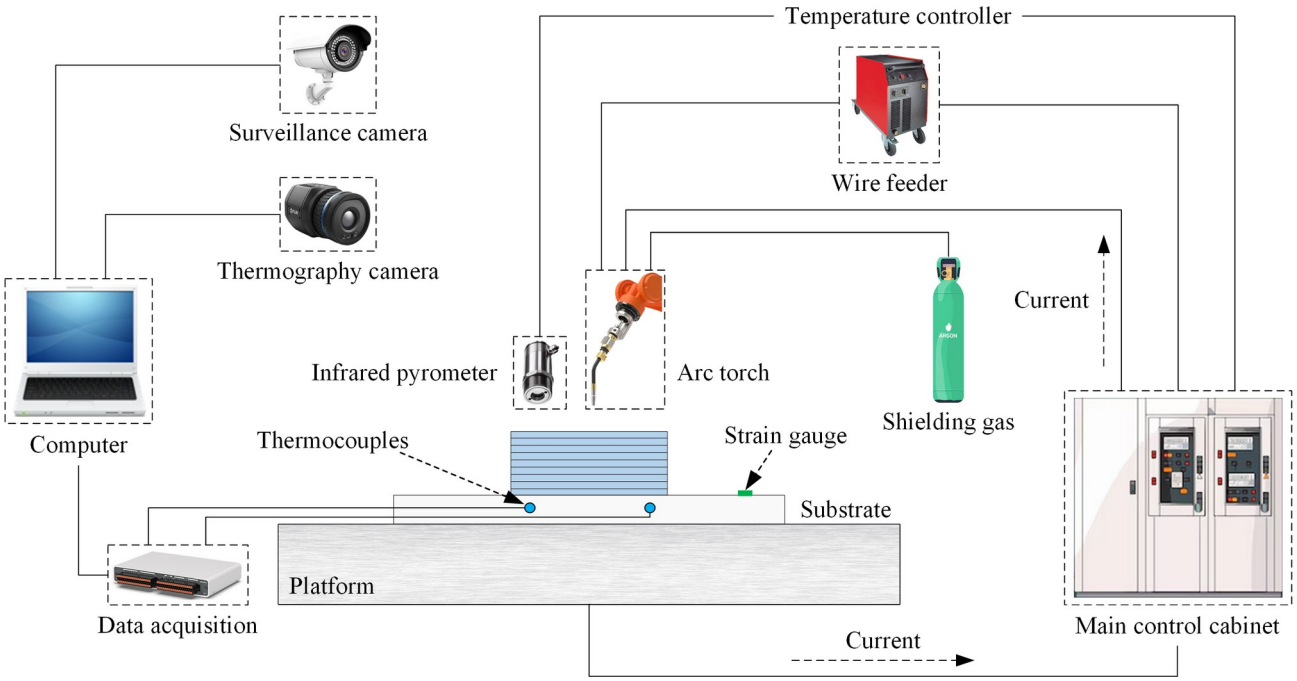


Fig. 1 Schematic of the experimental system.

Table 1 Chemical compositions (wt.%) of the wire feed and substrate.

| Materials | C | Si | Mn | P | S | Cr | Mo | Ni | Cu | Fe |
|---|---|---|---|---|---|---|---|---|---|---|
| Wire feed (AM35) | 0.09 | 0.30 | 1.08 | 0.006 | 0.005 | 0.04 | 0.01 | 0.03 | 0.06 | Bal. |
| Substrate (S355) | 0.17 | 0.35 | 1.20 | 0.014 | 0.001 | 0.04 | 0.004 | 0.25 | 0.22 | Bal. |

Table 2 Mechanical properties of the wire feed and substrate measured and provided by the supplier.

| Materials | Yield strength [MPa] | Ultimate tensile strength [MPa] | Failure elongation [%] |
|---|---|---|---|
| Wire feed (AM35) | > 355 | 470 ~ 630 | > 22 |
| Substrate (S355) | 399 | 534 | 33 |

## 2.2 Specimen preparation

Are shown in Fig. 2, the designed dimensions of the specimen are 160 mm × 40.8 mm × 66 mm, and it consisted of 22 layers, each 3 mm thick. Each layer contains 12 passes, each with a width of 3.4 mm. These dimensions were chosen to ensure the specimen was sufficiently high to accurately capture stable temperature and stress magnitudes. As depicted in Fig. 3, a reciprocating deposition trajectory was employed for ensuring uniform cooling and mitigating residual stresses within the part, where the endpoint of one layer is the starting point for the next. The arc torch travelled at a speed of 0.8 m/min, while the wire feed speed was set to 6.8 m/min, with a contact tip to work distance of 12 mm. The voltage and current waveforms, shown in Fig. 4, indicate an average deposition power of 4658 W. These process parameters were adjusted iteratively to achieve stable and high-quality builds. Shielding gas, composed of 92% Ar and 8% $CO_2$, was supplied at a flow rate of 16 L/min. An idle time of 4.4 s was applied between adjacent layers. During the experiment, the substrate was bolted to the platform using a torque wrench, achieving a pretension force of 10.2 kN. The entire process was conducted at an ambient temperature of 17 ℃.

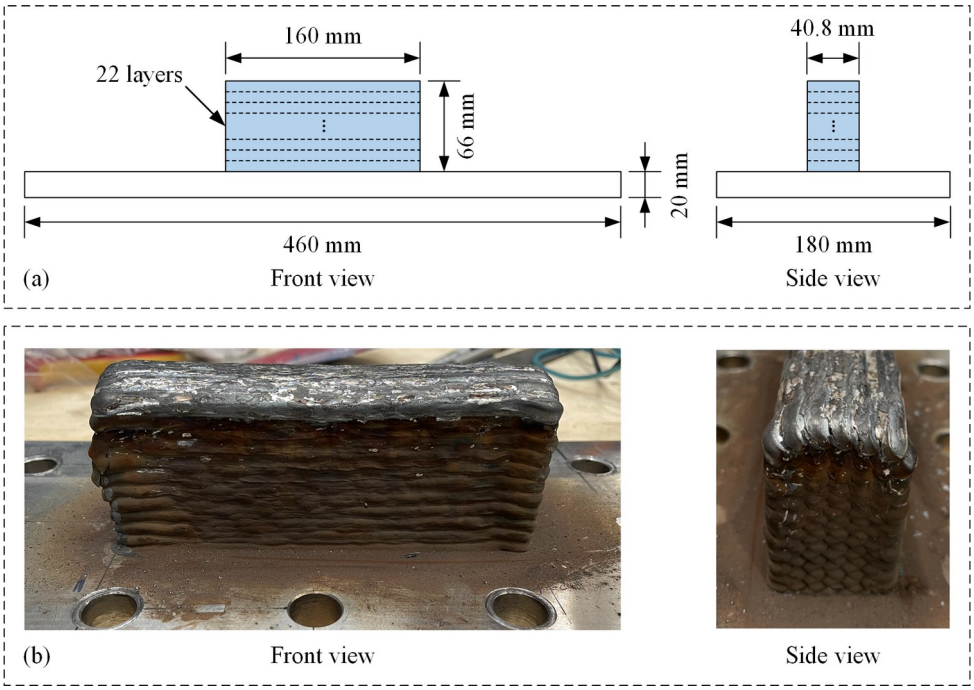


Fig. 2 Schematics of: (a) Dimensions [mm] of specimen; and (b) As-deposited component.

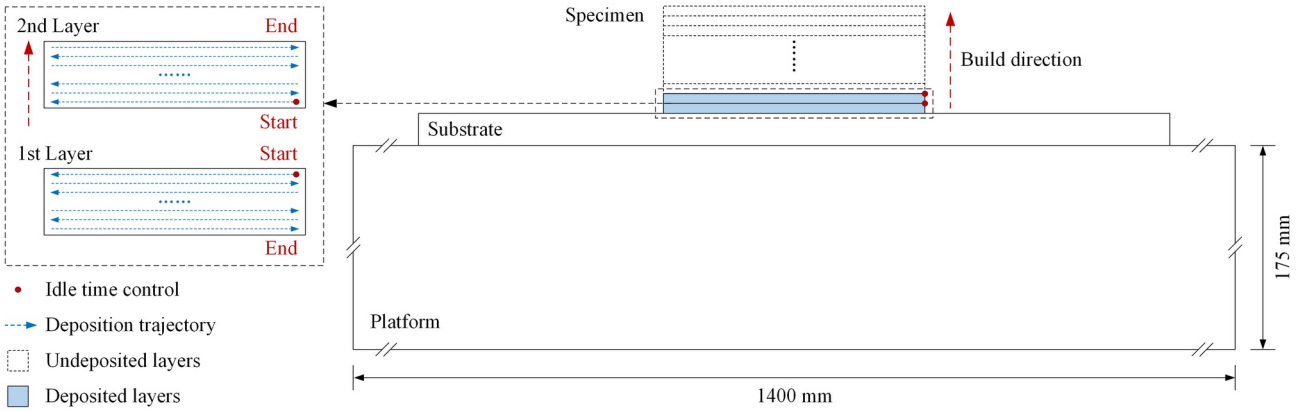


Fig. 3 Reciprocating deposition trajectory of the WAAM process.

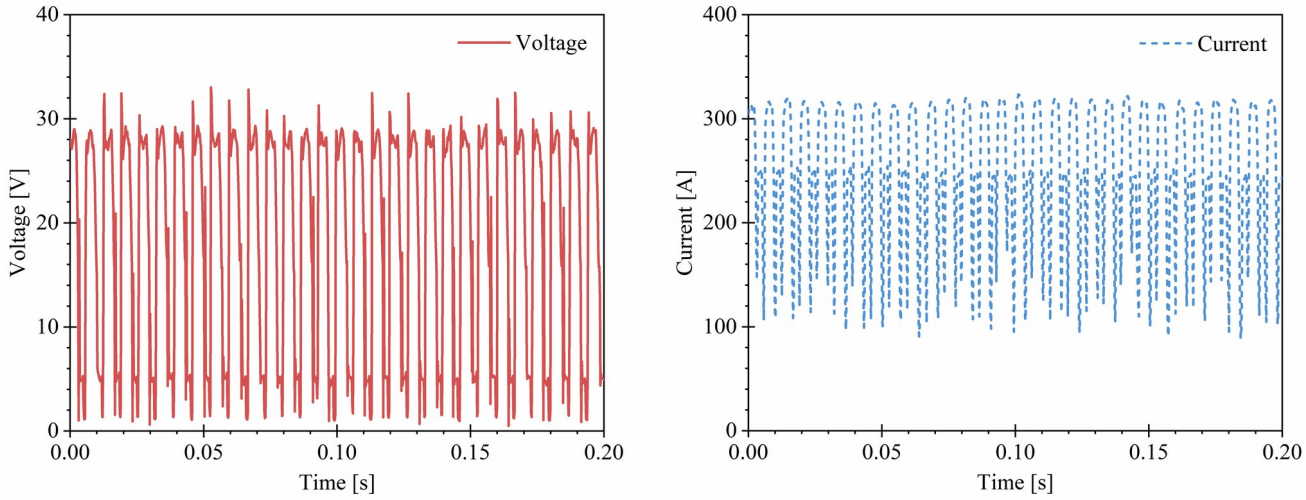


(a) Voltage waveform (b) Current waveform

Fig. 4 Voltage and current waveforms of the WAAM process.

## 2.3 Temperature measurements

As shown in Fig. 1, a model A700 FLIR thermography camera was used to monitor the thermal field development throughout the experiment. In addition, 10 K-type thermocouples (TCs) were soldered onto the substrate at specific locations to record temperature evolutions, as depicted in Fig. 5. The locations were chosen to capture temperatures on the top surface of the substrate, and at the bottom through the thickness, allowing a uniform representation of the temperature profile across the workpiece and its substrate. The thermocouples have a temperature range of -270 to 1260 ℃, with an accuracy of ±0.75%. The coordinates of the thermocouples, represented by blue squares, are schematically depicted in Fig. 5(b). The thermocouples were arranged in the following groups to capture comprehensive thermal histories across key regions: TC1 to TC4 were embedded along the longitudinal centreline of the substrate to measure thermal cycles at different depths (4 mm and 8 mm). TC5 and TC6 were positioned along the longitudinal fusion line to capture thermal histories

at different locations (centreline and corner). TC7 and TC8 were placed along the transverse direction to record temperature evolution at varying distances from the deposited specimen. Lastly, TC9 and TC10 were located along the longitudinal centreline of the deposit to monitor temperature changes at different longitudinal positions.

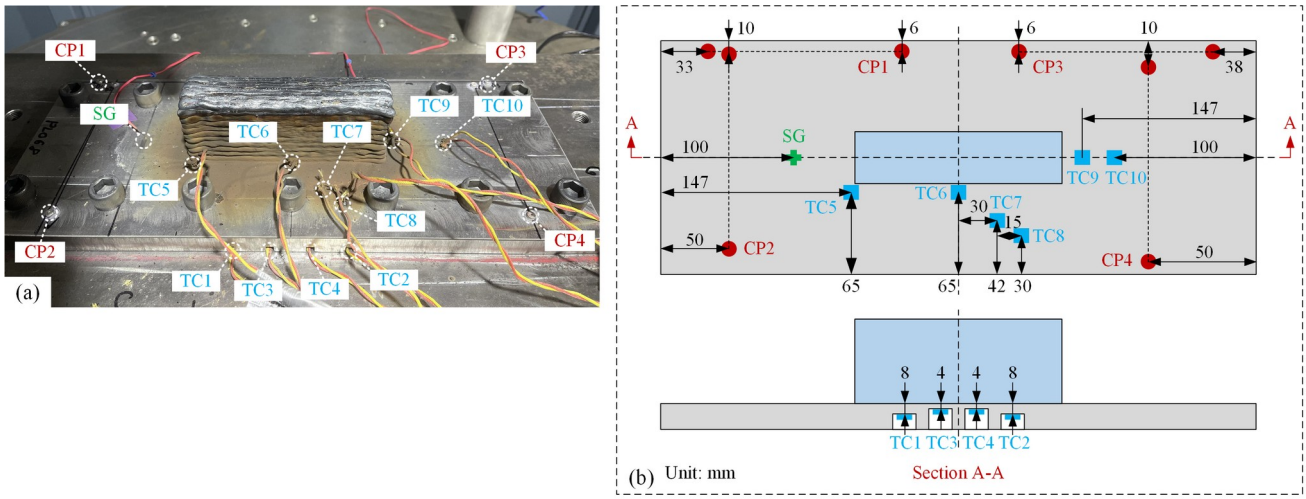


Fig. 5 (a) Installations and (b) Coordinates [mm] of TCs, SG and CPs on the specimen.

## 2.4 Strain and distortion measurements

A linear strain gauge (SG) was attached to the upper surface of the substrate to monitor strain evolution during the deposition, cooling, and unclamping processes. The strain gauge works within a normal temperature range of -10 to 80°C and has strain limits of 5%. The position of the SG, indicated by a green cross, is shown in Fig. 5(b). The gauge measured the transverse strain along the longitudinal centreline, and the measured strain was converted to stress values using Hooke's law. To evaluate the distortion of the specimens after unclamping (i.e., releasing the bolts), a three-dimensional (3D) laser scanner (3D Design FARO Scan Arm) was used, as depicted in Fig. 6. The scanned model was saved in STL format, containing vertices and triangular meshes. To ensure the accuracy of the 3D scanning, four groups of calibration points (CPs), spaced 150 mm apart, were established on the substrate's top surface, as shown in Fig. 5(b). The relative measurement errors for distances of CP1 to CP4 were 0.287%, 0.367%, 0.386% and 0.365%, respectively, confirming the high precision of the scanning for capturing the overall geometry.

To manage the large data-sets of scanned vertices and triangular meshes, Zuo et al. [43,44] developed a parametric analysis plug-in using Rhino-Grasshopper, which automatically generates virtual points to fit the external surface of 3D scanned models, enabling the extraction of geometric

details such as thickness at arbitrary locations. Similarly, this study introduces a MATLAB-based toolbox designed to capture the contours of scanned specimens at any chosen cross-sections and locations.

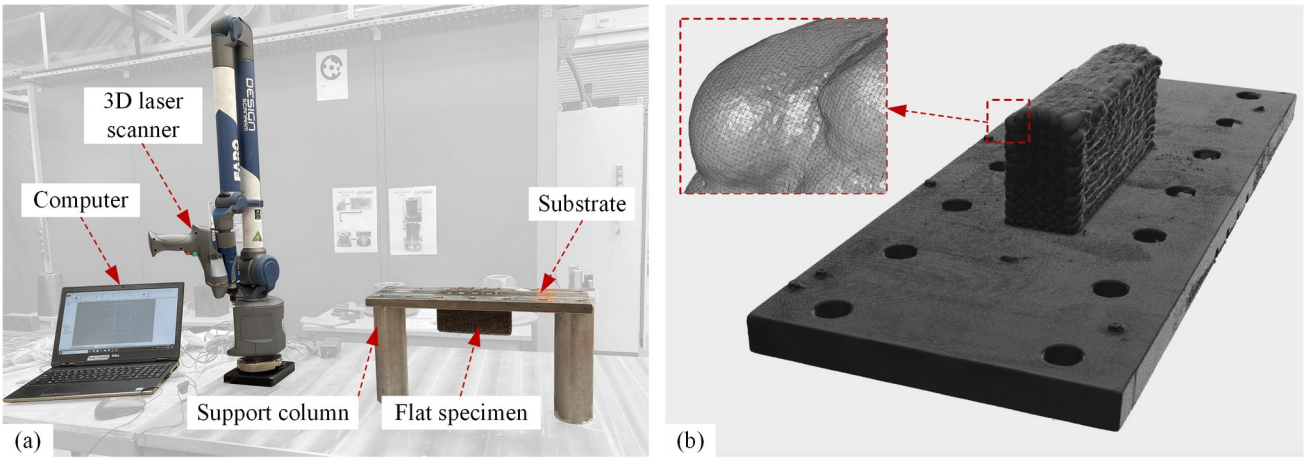


Fig. 6 Schematic of: (a) 3D laser scanning system; and (b) Corresponding scanned model.

## 2.5 Stress-strain curve

Three tensile coupons were machined from the deposited specimens in both the longitudinal (L1 – L3) and transverse (T1 – T3) directions, respectively. A schematic illustrating the locations and dimensions of these coupons is provided in Fig. 7. The tensile experiments were performed at ambient temperature using an Instron 1500 HDX series workbench. A strain rate of 0.00007 $s^{-1}$ was applied within the elastic range until reaching the proof strength, after which the strain rate was increased to 0.00025 $s^{-1}$ until failure. A video extensometer measured the stress-strain response by tracking the average strain field within the gauge length of each coupon.

The engineering stress-strain curves for both longitudinal and transverse coupons are presented in Fig. 8. Key mechanical properties including elastic modulus $E$, yield strength $f_y$, ultimate tensile strength $f_u$, ultimate strain $\varepsilon_u$, and total strain at failure $\varepsilon_f$ were determined following the method outlined in [45]. As some curves didn't exhibit a sharply-defined yield point, the 0.2% proof stress was used to define the yield strength, in accordance with [46]. The experimental results are summarised in Table 3, aligning well with values reported in previous studies [47–50]. For longitudinal coupons, the average $f_y$, $f_u$, $\varepsilon_u$, and $\varepsilon_f$ were 303.6 MPa, 442.9 MPa, 21.2% and 50.9%, respectively. For transverse coupons, the corresponding values were 313.2 MPa, 431.7 MPa, 20.4%, and 45.1%. While no significant anisotropy was observed in $f_y$, $f_u$ and $\varepsilon_u$, the longitudinal coupons

exhibited a notably higher $\varepsilon_f$ compared to the transverse coupons (i.e., 50.9% versus 45.1%). The highest tensile strength was observed in L1, likely due to microstructural anisotropy along the deposition height [51], where directional variations in grain structure and thermal history along the deposition height were shown to influence mechanical performance. Across all coupons, the average $f_y$ and $f_u$ were 308.4 MPa and 437.3 MPa, respectively.

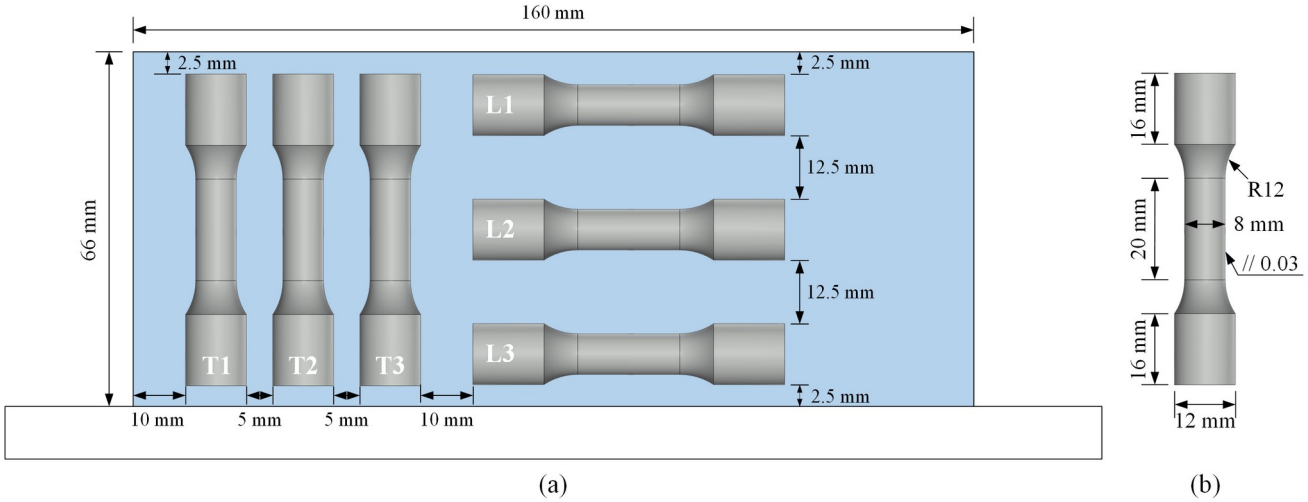


Fig. 7 Schematic of testing coupon preparation: (a) Locations of tensile coupons; and (b) Dimensions of tensile coupons.

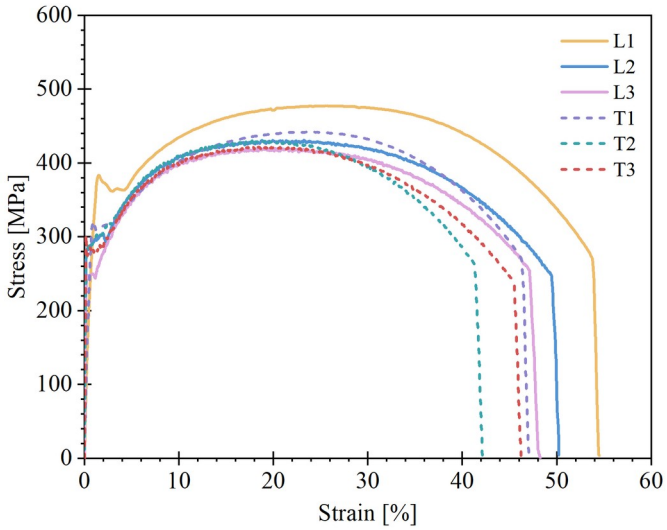


Fig. 8 Engineering stress-strain curves.

Table 3 Tensile test results based on video extensometer.

| Tensile coupons | $E$ [GPa] | $f_y$ [MPa] | $f_u$ [MPa] | $\varepsilon_u$ [%] | $\varepsilon_f$ [%] |
|---|---|---|---|---|---|
| L1 | 209.3 | 383.6 | 477.7 | 25.7 | 54.4 |
| L2 | 227.8 | 283.4 | 431.2 | 18.8 | 50.2 |
| L3 | 208.5 | 243.8 | 419.9 | 19.0 | 48.1 |
| Average | 215.2 | 303.6 | 442.9 | 21.2 | 50.9 |
| T1 | 215.8 | 344.6 | 442.2 | 24.2 | 47.1 |
| T2 | 229.3 | 283.4 | 431.0 | 17.7 | 42.1 |
| T3 | 203.4 | 311.6 | 422.0 | 19.4 | 46.2 |
| Average | 216.2 | 313.2 | 431.7 | 20.4 | 45.1 |

## 3 Finite element modelling

Three-dimensional coupled thermal-mechanical FE models based on a transient method are developed in this section to simulate the evolutions of temperature, stress, and deformation during the WAAM process. Comprehensive details about the thermal and mechanical modelling, heat source model and finite element mesh and computational settings are provided.

### 3.1 Thermal modelling

The energy equation governing the computational domain is expressed as Equation (1) [52]:

$$\frac{\partial\left(\rho C_P T\right)}{\partial t}=\frac{\partial}{\partial x}\left(k\frac{\partial T}{\partial x}\right)+\frac{\partial}{\partial y}\left(k\frac{\partial T}{\partial y}\right)+\frac{\partial}{\partial z}\left(k\frac{\partial T}{\partial z}\right)+Q \quad (1)$$

where $(x, y, z)$ are the coordinates of each node in the reference system, $T$ is the corresponding temperature at the node, $t$ is the system time, $\rho$ is the temperature-dependent density, $C_P$ is the specific heat capacity, $k$ is the thermal conductivity, and $Q$ represents the heat source term. Similar to [8], the temperature-dependent physical and mechanical properties of the deposited wall used in the FE model were simulated using JMatPro software based on its chemical compositions and tensile properties [53]. The results are presented in Fig. 9. For this analysis, heat and mass transfer phenomena within the molten pool are neglected.

Heat loss due to radiation and convection at the component's surface is modelled using Equation (2).

$$q-k\frac{\partial T}{\partial \vec{n}}=\varepsilon\sigma\left(T-T_0\right)^4+h\left(T-T_0\right) \quad (2)$$

where $q$ is the surface heat flux, $\vec{n}$ is the unit vector normal to the boundary surface, $\varepsilon$ is the grey body radiation coefficient (0.73), $\sigma$ is the Stefan-Boltzmann constant, and $h$ is the heat convection coefficient of 20 W/(m$^2$K) [8,54]. $T_0$ represents the ambient temperature, set at 290.15 K, and $T$ is the temperature at the surface nodes. To model cooling through the platform, the reference heat exchange coefficients from [8,22,41,42] are varying substantially. Based on a sensitivity assessment, it was demonstrated that adopting the heat exchange coefficient recommendation by [8,22], i.e., 300 W/(m$^2$K) for the substrate's bottom surface, provided the most accurate simulation results.

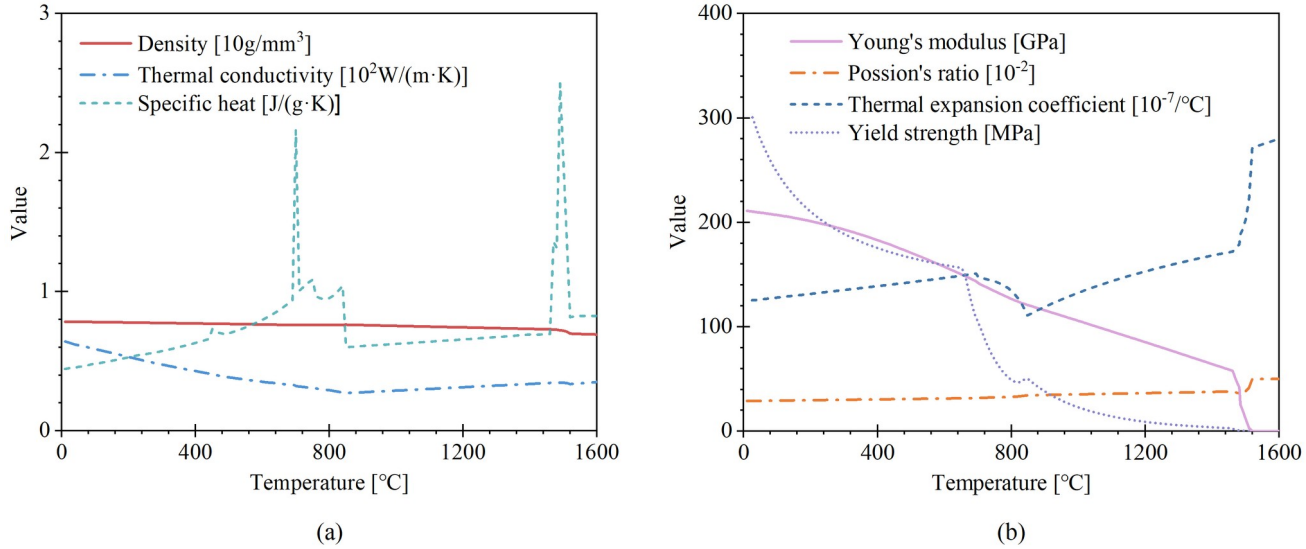


Fig. 9 Simulated temperature-dependent properties of the deposited wall: (a) Physical properties; and (b) Mechanical properties.

## 3.2 Mechanical modelling

The mechanical problem is governed by the balance of momentum equation, expressed in Equation (3):

$$\nabla \cdot \sigma + f = 0 \tag{3}$$

where $\sigma$ denotes the stress tensor and $f$ represents the body force vector.

For low carbon steels, the effect of phase transformation on residual stress is generally minor and can often be neglected in FE simulations. This is because cooling-induced microstructural evolution is dominated by diffusional transformations (i.e., austenite to ferrite/pearlite [7]), which involve small volumetric change and limited transformation-induced plasticity. Studies have shown that for steels with carbon content below 0.1 wt.%, residual stress development is primarily governed by thermal and mechanical responses rather than phase transformations, making elastic-plastic thermal models sufficiently accurate for engineering applications [55–58]. Consequently, the total strain tensor is described by Equation (4):

$$\varepsilon = \varepsilon_e + \varepsilon_p + \varepsilon_t \tag{4}$$

where $\varepsilon_e$, $\varepsilon_p$, and $\varepsilon_t$ correspond to the elastic, plastic, and thermal strain tensors respectively. A temperature dependent elastic-plastic material model is used for the analysis. The thermal strain $\varepsilon_t$ is calculated using Equation (5):

$$\varepsilon_t = \int_{T_0}^{T} \alpha_t \, dt \tag{5}$$

where $\alpha_t$ is the temperature dependent thermal expansion coefficient.

The trial stress, $\sigma^{tr}$, is calculated under the assumption that all strains are elastic, as shown in Equation (6):

$$\sigma^{tr} = C : \varepsilon \tag{6}$$

The deviatoric part of the trial stress, $\sigma^{tr'}$, is determined using Equation (7):

$$\sigma^{tr'} = \sigma^{tr} - \frac{I}{3}\left(\sigma^{tr} : I\right) \tag{7}$$

The von Mises trial stress, $\sigma_{VM}^{tr}$, which serves as a scalar measure driving plasticity, is calculated from the deviatoric part of the trial stress $\sigma^{tr'}$ using Equation (8):

$$\sigma_{VM}^{tr} = \sqrt{\frac{3}{2}\sigma^{tr'} : \sigma^{tr'}} \tag{8}$$

The plastic flow direction, $n_P$, is determined based on the trial deviatoric stress, following the principle of normality, as expressed in Equation (9):

$$n_P = \frac{3\sigma^{tr'}}{2\sigma_{VM}^{tr}} \tag{9}$$

The plastic strain is calculated using Equation **(10)**:

$$\varepsilon_p = n_P p \tag{10}$$

where $n_P$, is the flow direction and $p$ is the plastic strain increment.

The plastic strain is linked to the stress through the flow rule or yield function, $\Psi$, which depends on temperature. Therefore, during plasticity, Equation (11) should be satisfied.

$$\Psi\left(\sigma, p\right) = \sigma_{VM}^{tr} - \sigma_y\left(p, T\right) = 0 \tag{11}$$

### 3.3 Double ellipsoidal heat source model

In the transient analysis, the deposition heat source was implemented in the DFLUX subroutine using a moving heat source model. Various heat source models are available for WAAM simulations. For instance, Yang et al. [59] employed a hemisphere model due to its simplicity, minimal calibration requirements, and suitability for shallow deposits or thin-walled WAAM structures. However, hemisphere model has several limitations: it cannot capture the asymmetry of actual arc movement, performs poorly in modelling penetration, tends to overestimate surface temperatures, and lacks accuracy in multi-layer builds where heat accumulation and depth control are

critical. To address these issues, the Goldak's double-ellipsoidal heat source model is adopted in this study to simulate the heat input during the WAAM process [16]. It more accurately represents the heat input in both surface and depth, is adjustable to match experimental melt pool geometry, and is better suited for multi-layer WAAM processes requiring deeper penetration and precise thermal control. In the Goldak's double-ellipsoidal heat source model, the heat input is divided into two regions: front and rear ellipsoids, each defined by their own geometric parameters. A schematic of the Goldak's double ellipsoidal heat source is shown in Fig. 10(a). The heat flux in the coordinate system $(x, y, z, t)$ is described by the following Equations (12) to (14):

$$Q_f(x, y, z, t) = \frac{6\sqrt{3} f_f \eta P}{a_f bc\pi\sqrt{\pi}} e^{\left(\frac{-3(x-vt)^2}{a_f^2} - \frac{3y^2}{b^2} - \frac{3z^2}{c^2}\right)} \tag{12}$$

$$Q_r(x, y, z, t) = \frac{6\sqrt{3} f_r \eta P}{a_r bc\pi\sqrt{\pi}} e^{\left(\frac{-3(x-vt)^2}{a_r^2} - \frac{3y^2}{b^2} - \frac{3z^2}{c^2}\right)} \tag{13}$$

$$f_f + f_r = 2 \tag{14}$$

where $P$ is the average deposition power, $\eta$ is the heat source efficiency set to 0.9 for this experimental system [54], $f_f$ and $f_r$ are the fractions of deposition power allocated to the front and rear ellipsoids respectively, $a_f$ is the front ellipsoidal length, $a_r$ is the rear ellipsoidal length, $b$ is the ellipsoidal width, $c$ is the ellipsoidal depth, $v$ is the travel speed, and $t$ is the time.

To ensure modelling accuracy, the double ellipsoidal heat source parameters were calibrated using experimental data from a single pass deposition test conducted under identical process parameters. Fig. 10(b) compares the cross-sectional geometry of the bead-on-plate deposition against the simulated results. The comparison demonstrates similar deposition contours and heat affected zones, indicating that the calibrated heat source parameters are effective for simulating thermal behaviour in the proposed FE model. However, the heat source model does not fully capture the deposition penetration profile. This limitation is attributed to the smooth geometry of the double ellipsoidal heat source model and the fact that it neglects molten pool flow effects. The parameter values used in the heat source model are provided in Table 4.

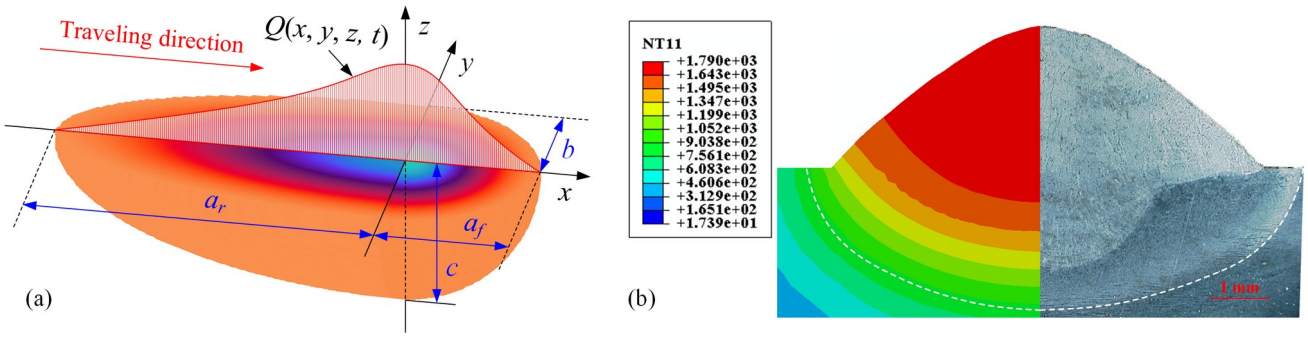


Fig. 10 Schematics of: (a) Goldak's double ellipsoidal heat source; and (b) Comparison of simulated thermal profile and experimental bead-on-plate cross-section.

Table 4 Parameters of double ellipsoidal heat source model.

| Parameter | $a_f$ [mm] | $a_r$ [mm] | $b$ [mm] | $c$ [mm] | $f_f$ [-] | $f_r$ [-] |
|---|---|---|---|---|---|---|
| Value | 4.0 | 11.0 | 3.6 | 4.0 | 0.6 | 1.4 |

### 3.4 Finite element mesh and computational settings

The FE model comprises four main components: the deposited specimen, substrate, platform, and bolts. The corresponding FE mesh is shown in Fig. 11. A mesh convergence study was performed in [8], evaluating FE mesh sizes of 1 mm, 2 mm, and 3 mm. The results demonstrated that a mesh size of 3 mm offers an optimal balance between computational efficiency and simulation accuracy. Detailed results and influence of mesh sizes on thermal and mechanical responses are summarised in the Appendix. The model includes 44,291 nodes and 37,216 elements. The deposited wall, bolts, and substrate were modelled using C3D8T solid elements, while the platform, with a thickness of 175 mm, was meshed using S4RT shell elements. To simulate the bolted connection, the nodes on the bolts' bottom surfaces were merged with the platform's top surface, and a pretension force of 10.2 kN was applied to the bolts. All contact surfaces were defined as surface-to-surface interactions with hard contact in the normal direction and a tangential friction coefficient of 0.3 commonly used for modelling friction between metals [8]. The platform's bottom edges were pinned to restrict movement. The origin ($O$) of the FE coordinate system was set at the centre of the bottom of the specimen.

The FE simulation was performed using the ABAQUS 2020 solver on a server equipped with two Intel® Xeon® CPU E5-2630 v3 2.40GHz processors, two NVIDIA Quadro P2000 graphic cards and 160GB of memory. The element birth and death technique was employed to simulate the material deposition process. Initially, the deposited wall elements were set to an inactive state and

were subsequently reactivated according to the arc torch's reciprocating motion pattern. The full Newton method was applied to solve the nonlinear equations, and automatic time control was used, with time increments ranging from $10^{-5}$ s and $10^{-2}$ s.

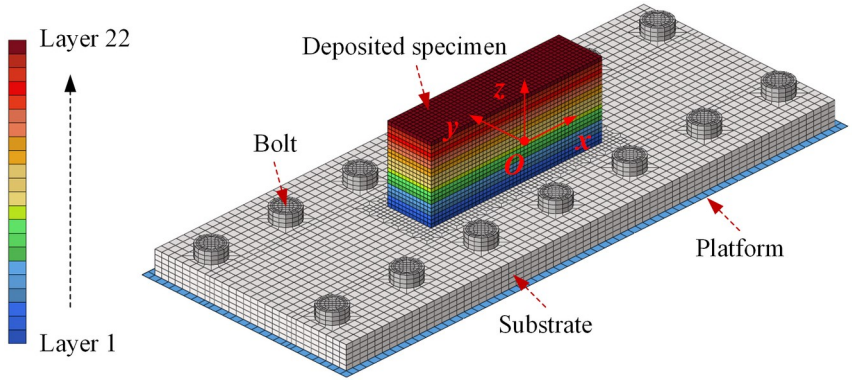


Fig. 11 Schematic of the FE model geometry and mesh.

## 4 Experimental validation

### 4.1 Temperature field

The temperature fields simulated by the FE model were compared with the experimental measurements from the thermography camera, as shown in Fig. 12. Representative frames were selected at specific deposition times: half-layer completions of the 5th, 10th, 15th, and 22nd layers, corresponding to $t_1$=797.5 s, $t_2$=1694.3 s, $t_3$=2591.1 s, and $t_4$=3846.6 s, respectively. Isotherms (white dashed lines) and corresponding temperature values are also indicated. The results demonstrate that the FE model accurately captures the evolution of the temperature field, showing strong agreement with the experimental data.

The analysis revealed that the temperature builds up as the deposition height rises as expected. For instance, regions with temperatures exceeding 1000 ℃, as well as molten pool regions (1500 ℃, shown as grey areas in the simulated thermal field) expand progressively with deposition. This behaviour is due to heat accumulation caused by the reduced heat sink effect provided by the platform as the deposition height increases [52,54]. Furthermore, significant temperature stratification is observed along the build direction within the deposited specimen. The accumulated heat effectively serves as a post-heat treatment for previously deposited layers. This finding suggests that appropriate cooling strategies could be employed to control and optimize the temperature field during the WAAM process. Such control may enhance the microstructure and mechanical properties

of the manufactured components, potentially eliminating the need for additional post-heat treatments [60,61].

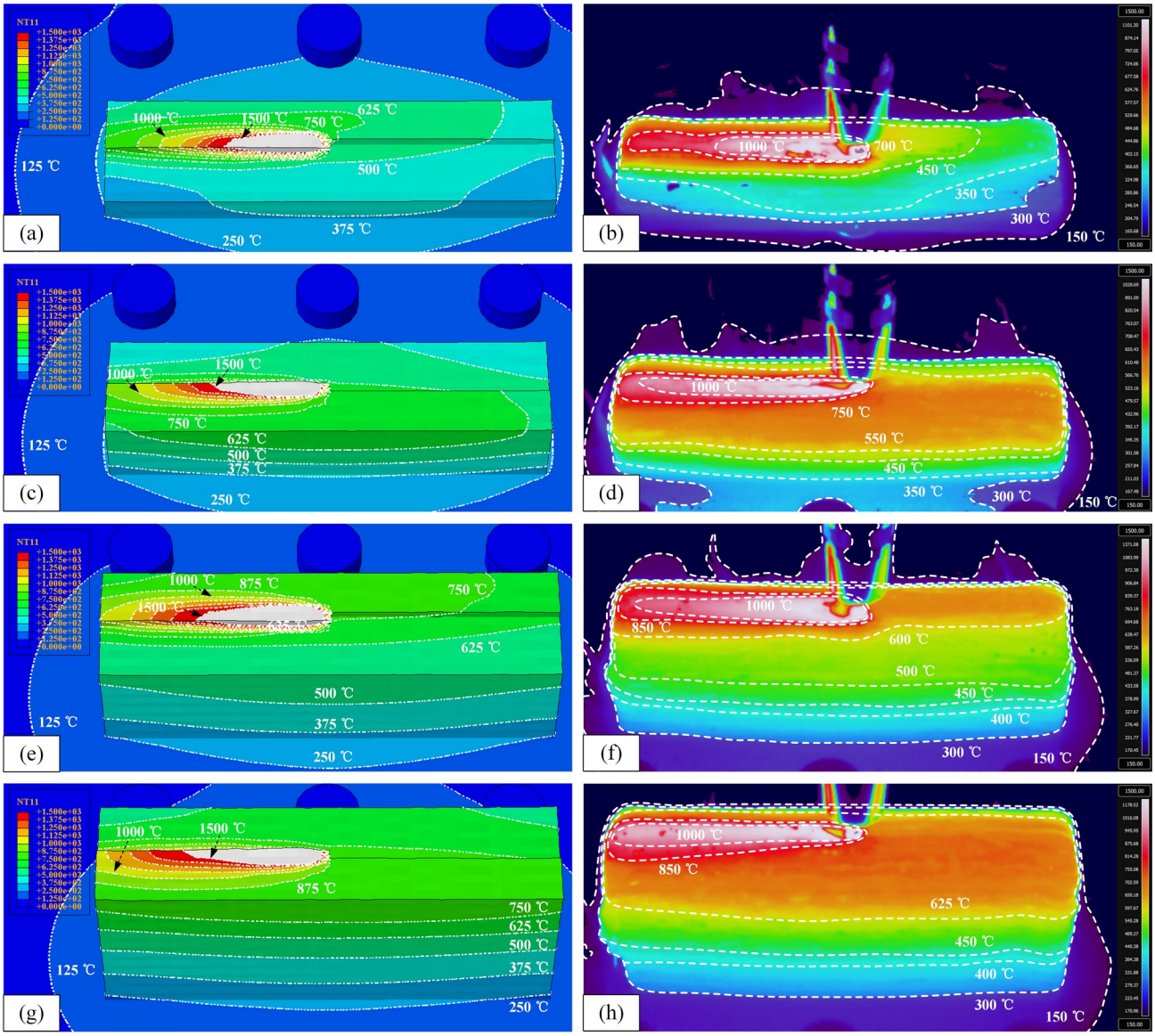


Fig. 12 Comparison of temperature fields between the FE model (left) and thermography images (right) for: (a, b) 5th layer ($t_1$=797.5 s); (c, d) 10th layer ($t_2$=1694.3 s); (e, f) 15th layer ($t_3$=2591.1 s); and (g, h) 22nd layer ($t_4$=3846.6 s).

The simulated temperature cycles at thermocouple locations of TC1 to TC10 were compared with experimental measurements, as shown in Fig. 13. To address the sparseness of FE nodes, a bilinear interpolation method was used to estimate the temperatures at the exact positions of the thermocouples based on the temperature values of adjacent nodes within the same element face.

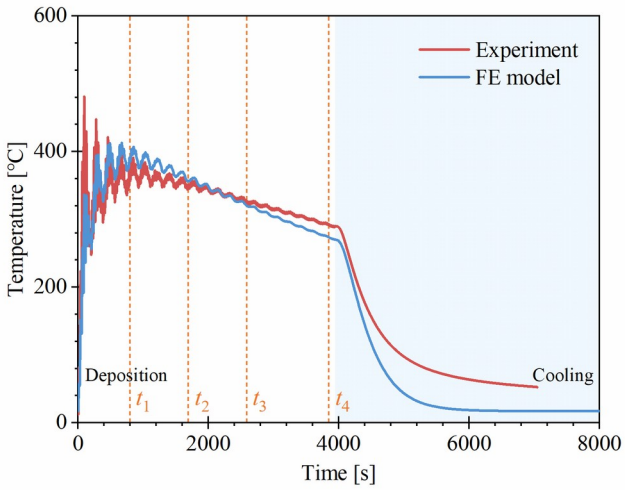


(a) TC1

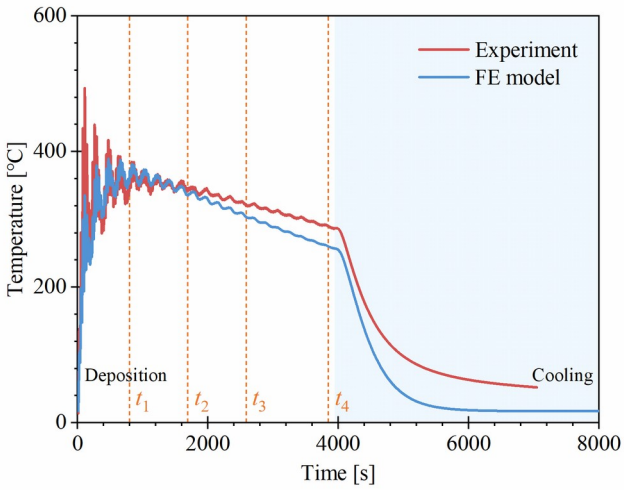


(b) TC2

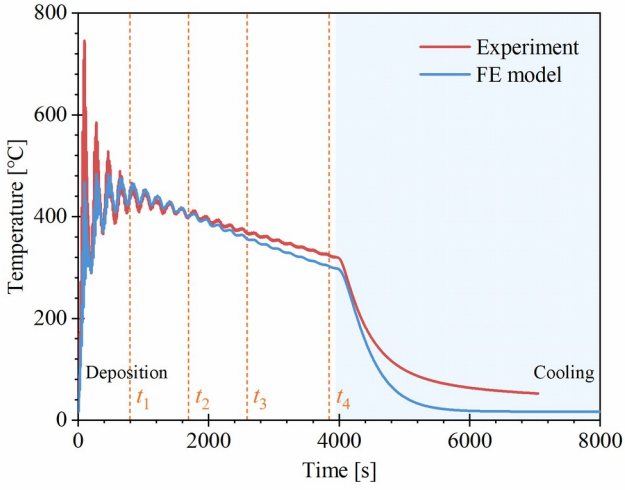


(c) TC3

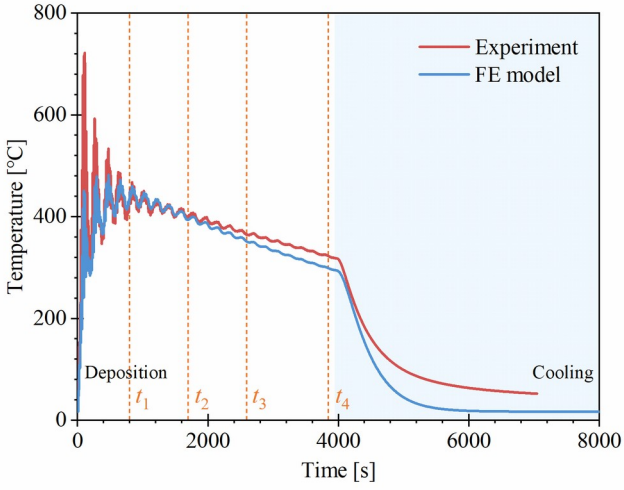


(d) TC4

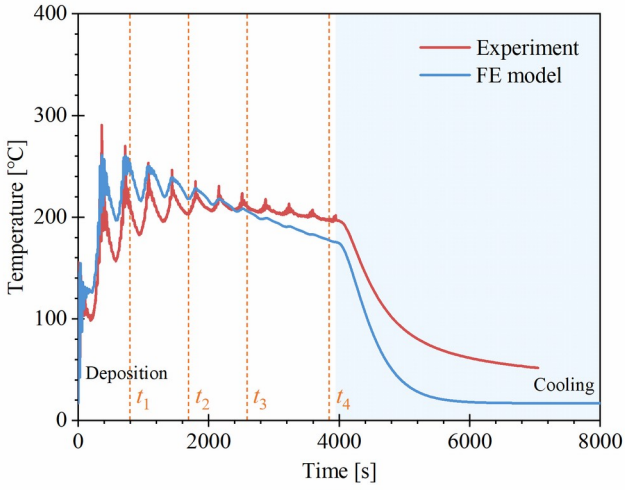


(e) TC5

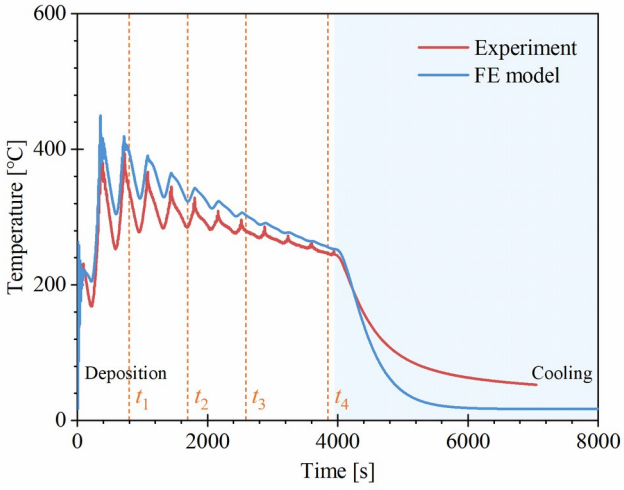


(f) TC6

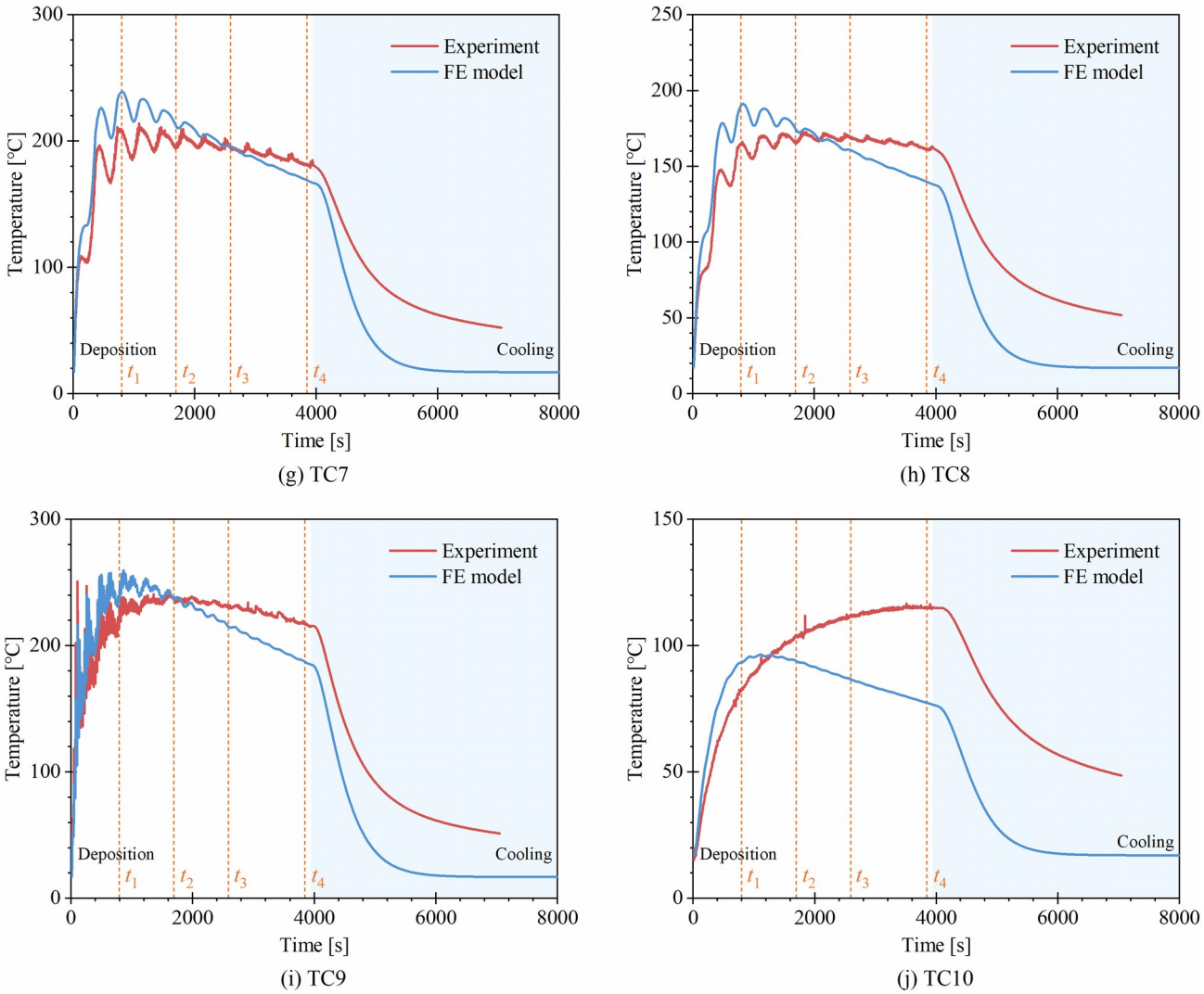


Fig. 13 Thermal cycles comparison between the experimental data and simulation results.

In Fig. 13, the thermal cycles are divided into two stages: the deposition stage (white region) and the cooling stage (blue region). The comparison displays a strong agreement between the simulated and measured thermal cycles, which reinforces both our hypotheses and the accuracy of our measurements. The periodic nature of the thermal cycles reflects the repeated motion of the WAAM heat source during the deposition process. The simulated and measured temperatures at the stages $t_1$ to $t_4$ are summarised in Table 5. For the embedded thermocouples (TC1 ~ TC4), the temperatures of TC3 and TC4 are higher than those of TC1 and TC2, due to their closer proximity to the deposition surface (4 mm versus 8 mm). The FE model achieves high simulation accuracy for TC1 ~ TC4, with the maximum relative simulation error being 10.2% at $t_4$ for TC2. For thermocouples located along the fusion line (TC5 and TC6), the model also achieves good accuracy, with maximum relative errors of 18.3% for TC5 and 16.2% for TC6. Along the transverse direction (TC7 and TC8, positioned at 42 mm and 30 mm, respectively), the thermal cycles predicted by the

model align closely with the experimental trends. TC9, being closer to the deposited wall, records higher temperatures compared to TC10. The timing of the peak temperature for TC10 varies significantly between the experimental measurements and the FE simulations (3507.1 s versus 1102.7 s), indicating that the model did not fully capture the heat accumulation at the far end of the substrate.

Overall, the FE model effectively replicates both the trends and values of the measured temperature cycles, accurately capturing the fluctuations and decrease in the thermal cycles. The observed discrepancies can be partially attributed to alignment errors during the installation of K-type thermocouples and the interpolation of simulated temperatures. These uncertainties, combined with the high temperature gradients, contribute to the observed measurement errors.

Table 5 Comparison of the measured and FE simulated temperatures at specific time frames.

| | | TC1 | TC2 | TC3 | TC4 | TC5 | TC6 | TC7 | TC8 | TC9 | TC10 |
|---|---|---|---|---|---|---|---|---|---|---|---|
| $t_1$ | Expt. [℃] | 361.4 | 357.2 | 437.7 | 429.2 | 212.1 | 340.8 | 209.1 | 165.1 | 229.0 | 82.9 |
| | FE [℃] | 390.2 | 360.2 | 444.0 | 435.1 | 250.9 | 396.1 | 238.9 | 190.2 | 243.3 | 93.3 |
| | RE [%] | 8.0 | 0.8 | 1.5 | 1.4 | 18.3 | 16.2 | 14.3 | 15.2 | 6.2 | 12.6 |
| $t_2$ | Expt. [℃] | 346.8 | 343.0 | 399.3 | 399.4 | 203.5 | 286.5 | 196.1 | 165.6 | 237.3 | 103.7 |
| | FE [℃] | 356.6 | 335.3 | 400.4 | 393.9 | 218.1 | 323.2 | 211.8 | 174.5 | 236.7 | 93.9 |
| | RE [%] | 2.8 | 2.2 | 0.3 | 1.4 | 7.2 | 12.8 | 8.0 | 5.4 | 0.3 | 9.5 |
| $t_3$ | Expt. [℃] | 323.4 | 321.3 | 367.3 | 365.3 | 210.3 | 280.1 | 195.5 | 168.9 | 231.4 | 111.9 |
| | FE [℃] | 319.7 | 303.1 | 356.0 | 351.3 | 205.9 | 302.9 | 196.0 | 160.8 | 215.0 | 86.7 |
| | RE [%] | 1.1 | 5.7 | 3.1 | 3.8 | 2.1 | 8.1 | 0.2 | 4.8 | 7.1 | 22.5 |
| $t_4$ | Expt. [℃] | 291.3 | 289.8 | 323.4 | 322.8 | 196.4 | 245.9 | 181.1 | 161.0 | 217.9 | 115.2 |
| | FE [℃] | 273.6 | 260.2 | 302.7 | 299.1 | 177.3 | 255.9 | 169.1 | 139.9 | 187.2 | 77.4 |
| | RE [%] | 6.1 | 10.2 | 6.4 | 7.4 | 9.7 | 4.1 | 6.7 | 13.1 | 14.1 | 32.8 |

## 4.2 Stress field evolution and residual stresses

To validate the accuracy of the simulated strain and stress evolution, the stress cycle (transverse stress S22 along the longitudinal centreline) recorded by the SG was compared with the FE simulation results, as shown in Fig. 14. The transient stress evolution is divided into three distinct stages: deposition (white region), cooling (blue region), and unclamping (white region). During the deposition stage, thermal stresses oscillate cyclically, driven by the temperature cycles and influenced by the deposition trajectory. In the cooling stage, stress intensities stabilize. The most significant changes in the stress field occur during the unclamping stage, when the bolts are removed, leading to springback effects. At the SG location (in the transverse direction along the longitudinal

centreline), the material predominantly experiences tensile stress. The maximum transient stress measured by the SG is 107.9 MPa, while the simulated value is 108.9 MPa, resulting in a relative error of 0.9%. The minimum measured transient stress is -13.5 MPa, compared to a simulated value of -17.4 MPa, giving a relative error of 29.1%. Table 6 summarises the simulated and measured stresses during the deposition stage ($t_1$=797.5 s, $t_2$=1694.3 s, $t_3$=2591.1 s, and $t_4$=3846.6 s), the fully cooled stage ($t_5$=8635.0 s), and the unclamping stage ($t_6$=9000.0 s). The FE model demonstrates high accuracy in simulating stress evolution across all stages, see Fig. 14 and Table 6. Overall, the FE model effectively reproduces the stress development trends and magnitudes across all three phases.

The deviations between the experimental measurements and the simulated thermal stresses can be attributed to two primary factors, alongside common testing inaccuracies. First, the SG installation location does not precisely align with the nodes in the FE mesh. Although bilinear interpolation was used to estimate stress values at the SG location, some interpolation error is also inevitable. Additionally, the high heat input during the process introduces measurement errors due to thermal expansion. Despite applying thermal compensation, these errors remain unavoidable under the extreme thermal conditions experienced during the experiment.

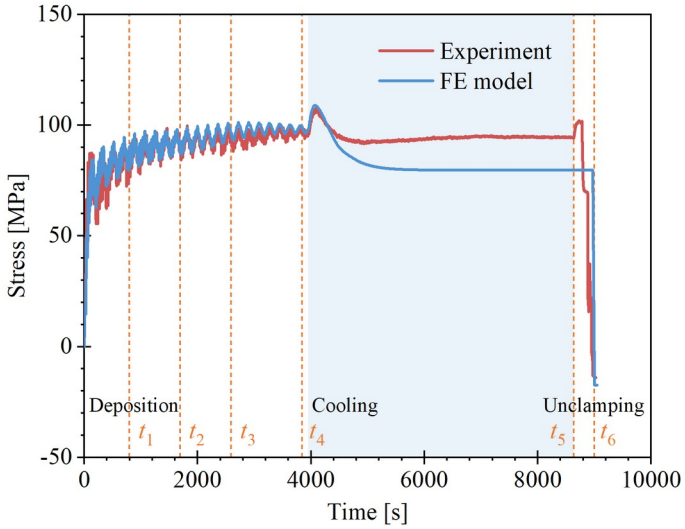


Fig. 14 Transient transverse stress (S22) comparison at SG between the experimental data and simulation results.

Table 6 Comparison of the measured and FE simulated transverse stresses (S22) at specific time frames.

| | $t_1$ | $t_2$ | $t_3$ | $t_4$ | $t_5$ | $t_6$ |
|---|---|---|---|---|---|---|
| Expt. [MPa] | 85.9 | 90.7 | 94.1 | 98.6 | 94.2 | -13.5 |
| FE [MPa] | 90.1 | 91.0 | 96.4 | 98.6 | 79.7 | -17.4 |
| RE [%] | 4.9 | 0.3 | 2.5 | 0.1 | 15.4 | 29.1 |

Fig. 15 shows the simulated von Mises stresses at different stages of the process, including the 5th, 10th, 15th, and 22nd layers, as well as the fully cooled stage, and the unclamping stage, corresponding to deposition times of $t_1$ to $t_6$. The results show that the maximum von Mises stresses increase with deposition height, rising from 338.2 MPa at the 5th layer to 462.3 MPa at the 22nd layer. High residual stress regions are primarily concentrated around the interface between the substrate and the deposited specimen. Moreover, these high-stress regions expand in size as the deposition height increases, reflecting the cumulative thermal and mechanical effects of the process. Following the removal of the bolts during the unclamping stage, the residual stress decreases, as part of the stress is relieved due to springback effects.

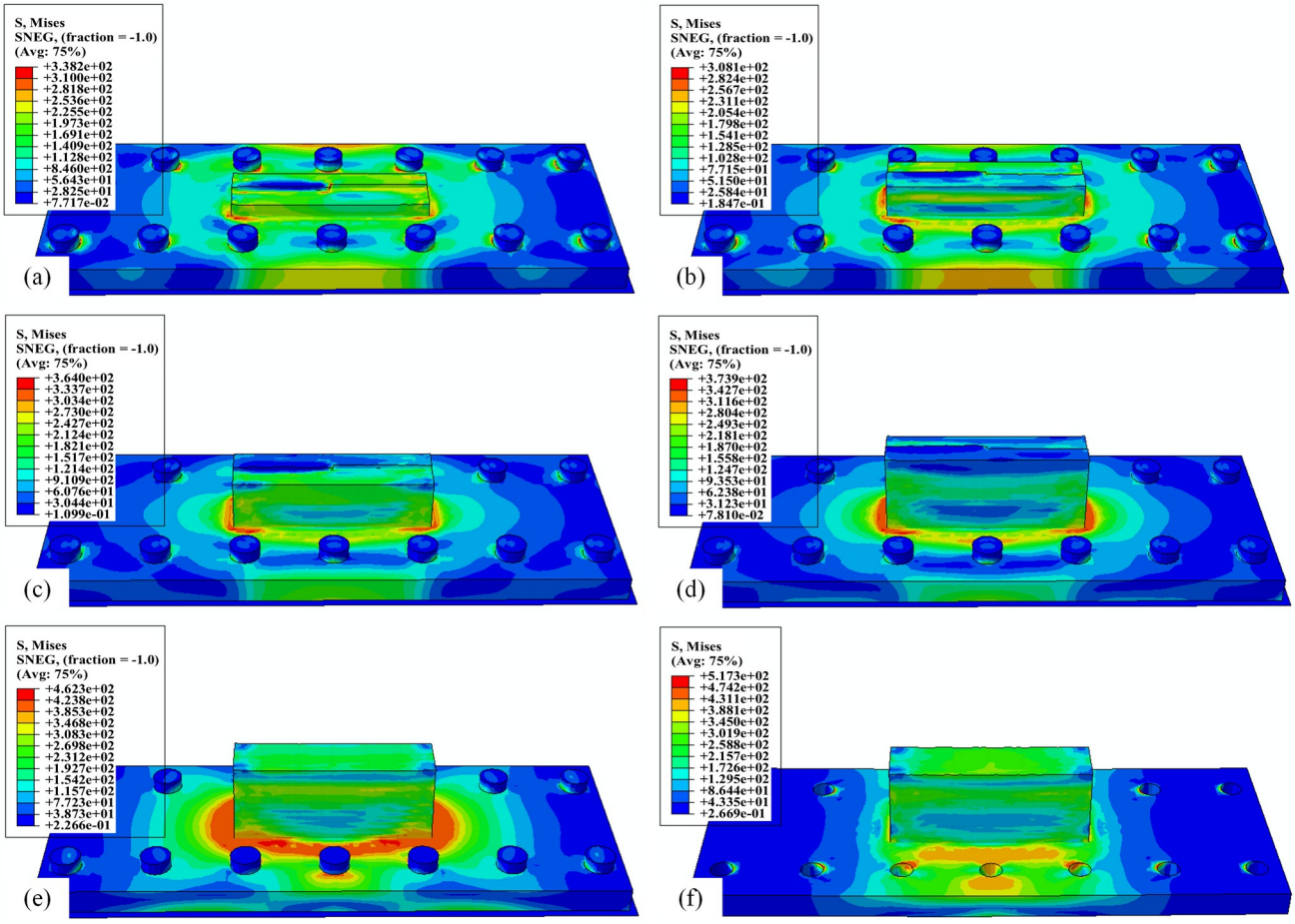


Fig. 15 FE simulated von Mises stresses at different stages: (a) 5th layer ($t_1$=797.5s); (b) 10th layer ($t_2$=1694.3s); (c) 15th layer ($t_3$=2591.1s); (d) 22nd layer ($t_4$=3846.6s); (e) Fully cooling stage ($t_5$=8635.0s); and (f) Unclamping stage

## 4.3 Residual stress distribution

To analyse the residual stresses in the specimens, the longitudinal residual stress (S11) and transverse residual stress (S22) were evaluated along lines AB, CD, and EF under clamping, unclamping and substrate removal conditions, as shown in Fig. 16. The letters on the side of the

curves indicate the endpoints of the lines, and the blue area indicates the area of the deposited flat specimen. The positions of these lines are also illustrated in Fig. 16: (1) Line AB represents the longitudinal centreline of the substrate's top surface (*x*-axis direction); (2) Line CD is parallel to the transverse centreline of the substrate's top surface (*y*-axis direction); and (3) Line EF is the vertical centreline passing through the substrate and deposited specimen (*z*-axis direction).

Along line AB, both longitudinal and transverse stresses vary significantly, peaking at the boundaries between the deposited specimen and the substrate. These stresses redistribute and drop noticeably after unclamping due to the release of bolt-induced constraints. Along line CD, stresses exhibit clear transitions as the line crosses the boundaries of the model. Stress redistribution caused by the bolt removal is also apparent, leading to important changes in both longitudinal and transverse stress profiles. Along line EF, clear stress transitions occur at the boundary between the substrate and the deposited specimen ($z$=0). Within the substrate, both longitudinal and transverse stresses exhibit dynamic behaviour, initially decreasing and then increasing. The longitudinal stress transitions from tension to compression, while the transverse stress follows a more complex pattern. The transverse stress exhibits an alternating tension-compression-tension-compression pattern from the bottom of the substrate (Point E) to the top surface of the deposited wall (Point F). A similar zig-zag stress distribution has also been reported by Yuan et al. [38], who observed that WAAM specimens, regardless of material, welding method or dimensions, can develop similar zig-zag residual stress patterns along their height, consistent with the results shown in Fig. 16(f). This complex behaviour is attributed to bending deflection, which induces tensile stress in the substrate and compressive stress on the top surface of the deposited specimen once the clamps are released. Stress redistribution along line EF after substrate removal is also shown in Fig. 16(e) and Fig. 16(f). The longitudinal stress decreases at the bottom ($z$=0) and increases at the top ($z$=66) of the deposited specimen. For transverse stress, the removal of the substrate primarily affects the residual stress in the first ten layers of the deposited wall, while the residual stresses in the remaining layers remain stable.

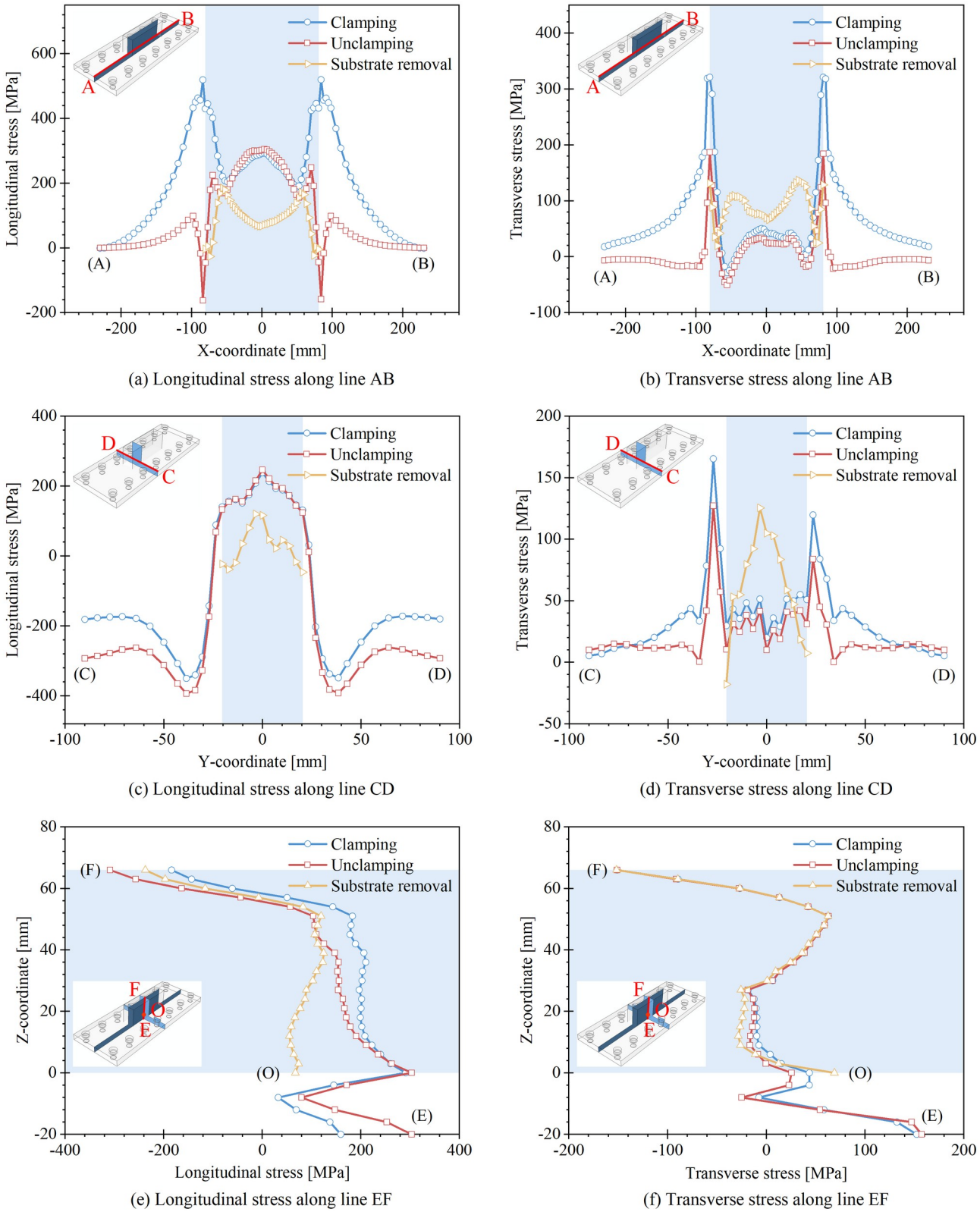


Fig. 16 Longitudinal and transverse residual stresses along the lines AB, CD and EF.

An overview of the simulated residual stress distribution within the specimen after unclamping is presented in Fig. 17. The red regions indicate tensile stress, while the blue regions represent compressive stress. In both sections Ⅰ and Ⅱ, the bottom region of the substrate experiences tensile longitudinal stress, while the top region of the deposited specimen is subjected to compressive

longitudinal stress, indicating bending deformation of the component after unclamping. Fig. 18 compares the 3D laser scanned deformed profiles with the simulated deformations of the flat specimen along lines GH and IJ at the substrate's bottom surface. The comparison shows strong agreement between the simulated and measured profiles, further validating the accuracy of the FE model.

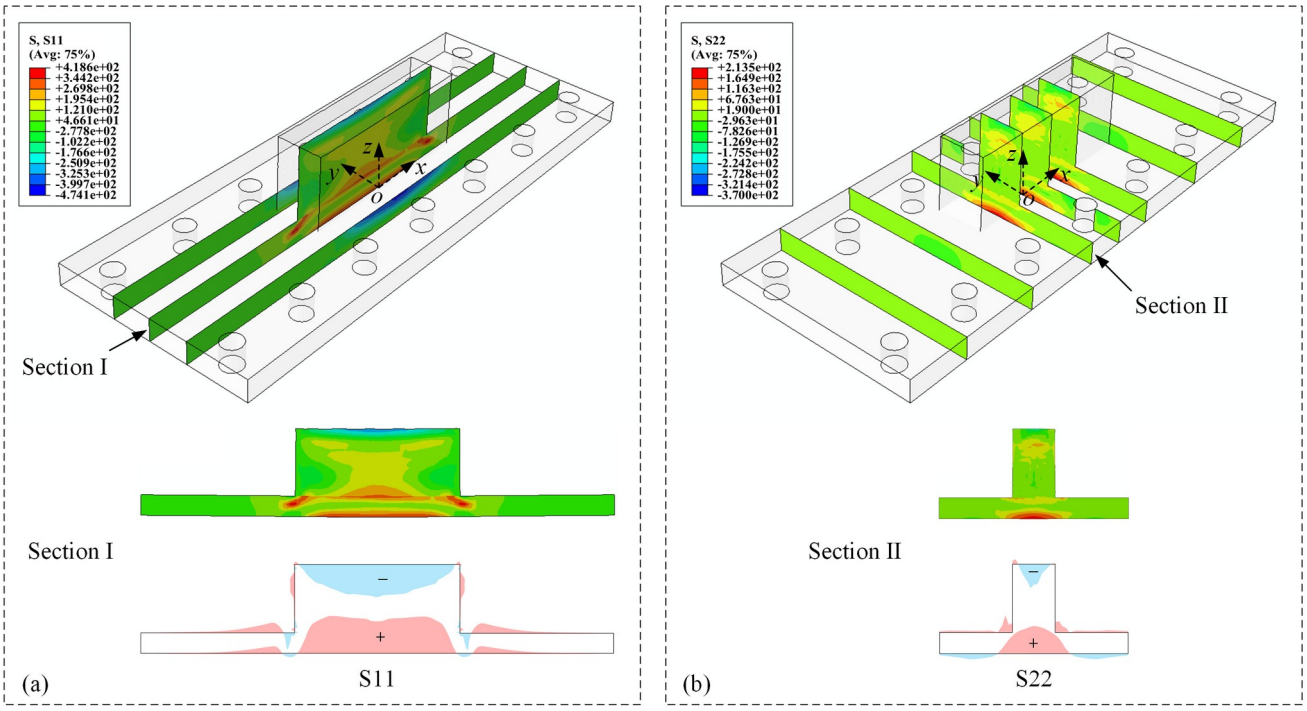


Fig. 17 Residual stress distributions after unclamping: (a) Longitudinal stress (S11); and (b) Transverse stress (S22).

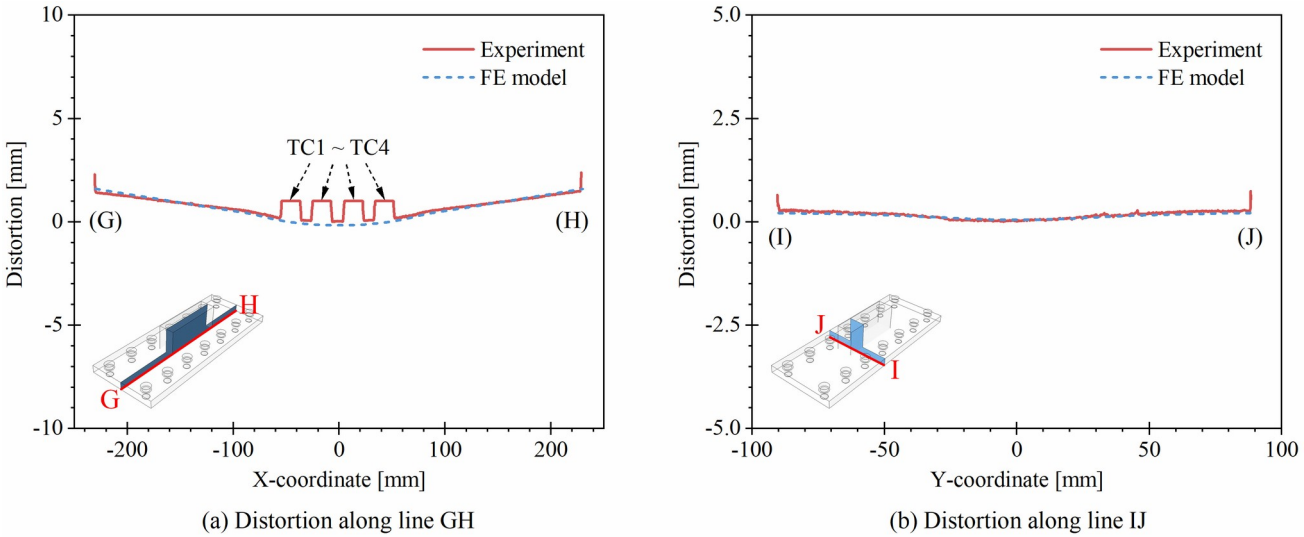


Fig. 18 Distortion of the flat specimen after unclamping along lines GH and IJ.

## 5 Case study

### 5.1 Model description

To further investigate the residual stress distributions in the specimens under varying scenarios, six additional cases with different number of deposited layers and boundary conditions were modelled. Case 1 to Case 4: These cases simulate specimens with different number of deposited layers, in steps of 5 layers up to 20 layers in total to investigate the temperature development and stress evolution in the specimen. The corresponding FE meshes for these cases are shown in Fig. 19. Case 5 and Case 6: These cases explore different platform concepts to reflect realistic manufacturing conditions. In Case 5, the platform underneath the substrate is disregarded. In contrast, Case 6 extends the substrate to include the platform underneath. These boundary conditions are consistent with methodologies adopted in previous research [62,63]. The FE meshes for Cases 5 and 6 are presented in Fig. 20. The details of the FE models for all simulated cases are summarised in Table 7. For reference, the FE model discussed in Sections 3 and 4 is referred to as Case 0.

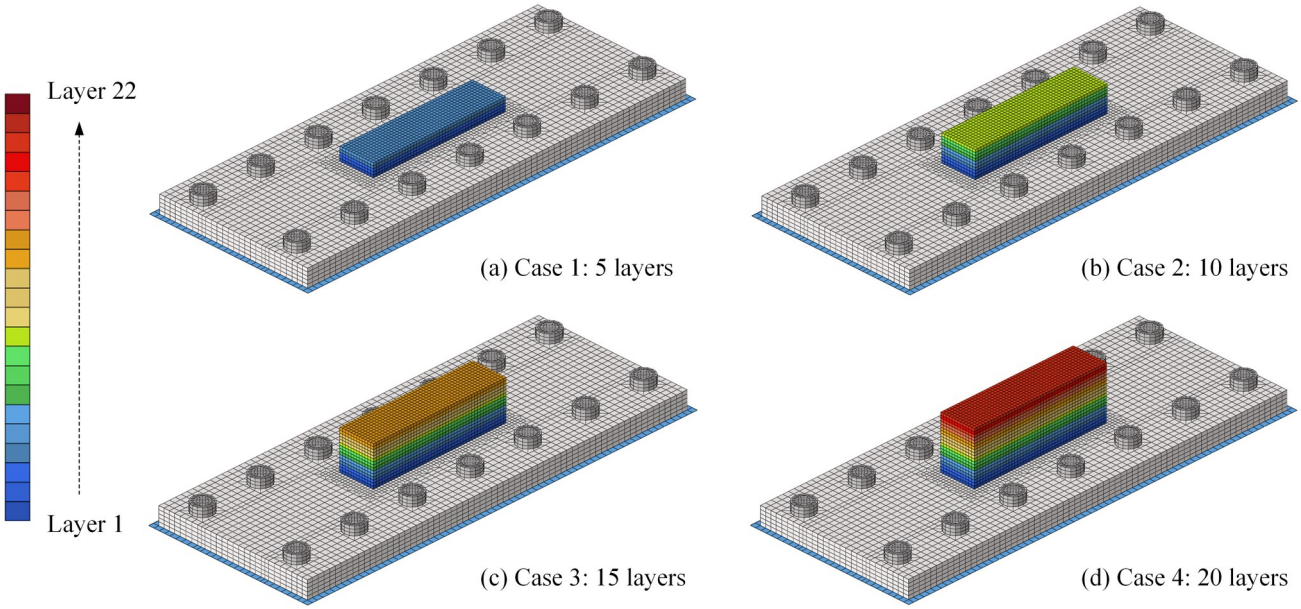


Fig. 19 FE meshes with different deposition layers.

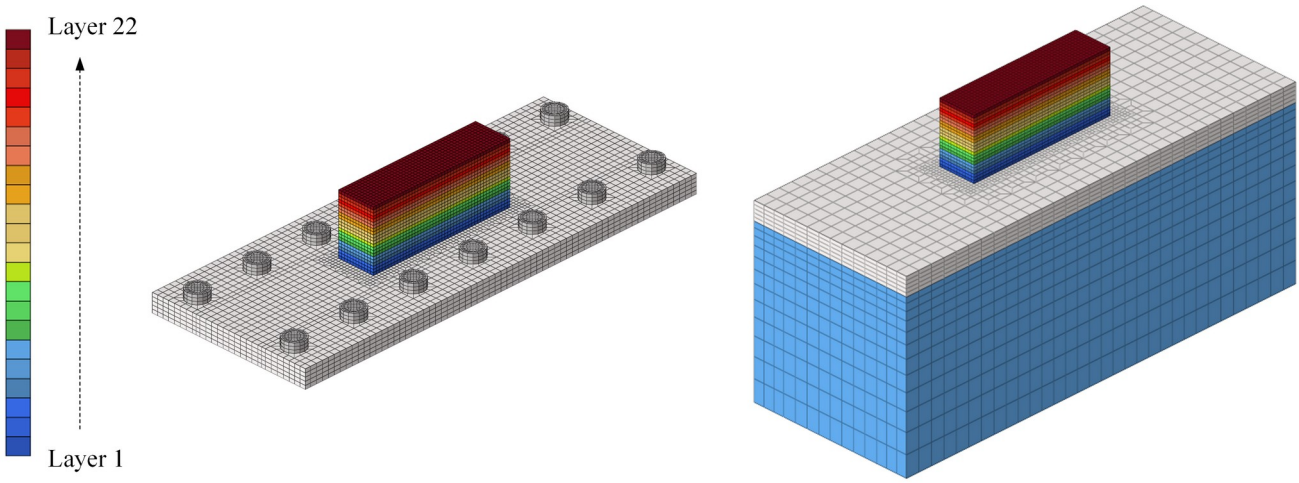


(a) Case 5: Platform concepts without platform (b) Case 6: Platform concepts without bolts

Fig. 20 FE meshes with different platform concepts.

Table 7 Details of the FE models for different simulated cases.

| Models | Layers | Boundary | Pretension force [kN] | Number of finite elements |
|---|---|---|---|---|
| Cases 0 | 22 | Platform and bolts | 10.2 | 37,216 |
| Cases 1 | 5 | Platform and bolts | 10.2 | 27,832 |
| Cases 2 | 10 | Platform and bolts | 10.2 | 30,592 |
| Cases 3 | 15 | Platform and bolts | 10.2 | 33,352 |
| Cases 4 | 20 | Platform and bolts | 10.2 | 36,112 |
| Cases 5 | 22 | Without platform | N/A | 33,064 |
| Cases 6 | 22 | Without bolts | N/A | 38,460 |

## 5.2 Influence of deposition layers

The simulated thermal cycles at TC1 and stress evolutions at SG for different deposition layers are presented in Fig. 21, and corresponding trends are shown in Fig. 22. The thermal analysis shows that all specimens, regardless of the number of layers, reach a peak temperature of 412.9 ℃ at 670.8 s, corresponding to 3.8 layers. As the number of deposition layers increases, the temperature at the end of the deposition process (finish deposition state in Fig. 22) decreases almost linearly, while the corresponding stress values remain relatively constant. Additionally, the peak stress in all cases occurs at the beginning of the cooling stage (finish deposition state) and is slightly higher than the final stress. After complete cooling (clamping state), stress levels increase at SG with additional layers, stabilizing at 20 and 22 layers. Once the structure is unclamped, the residual stress at SG drops significantly and transitions into compressive stress at a consistent level across all cases. This is because unclamping partially alleviates the substrate's residual stress caused by the deposition process.

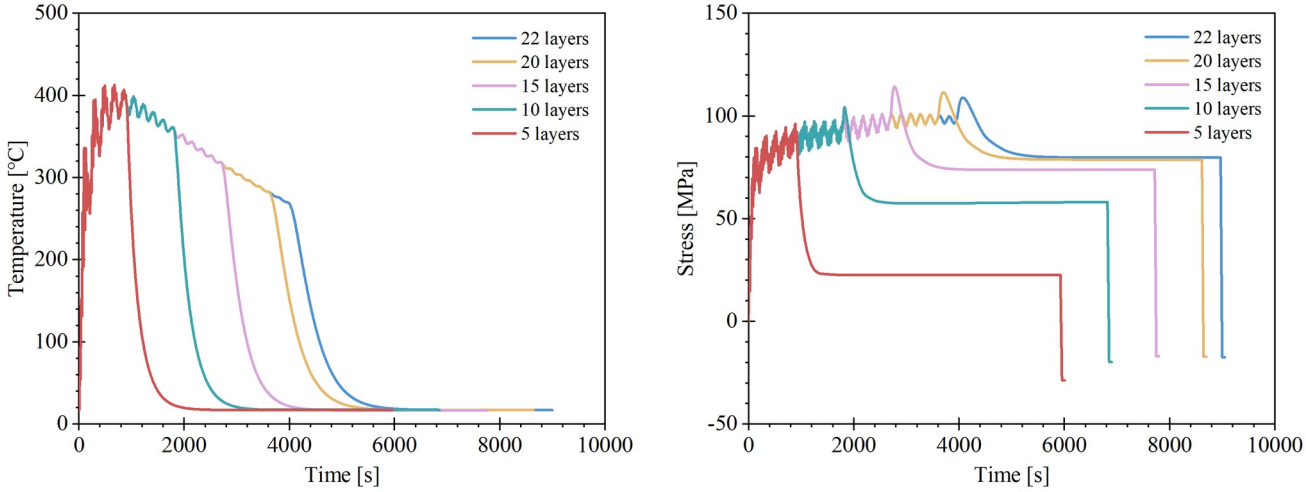


(a) Thermal cycles of TC1 (b) Stress evolutions of SG

Fig. 21 Simulated thermal cycles and stress evolutions for specimens with varying deposition layers.

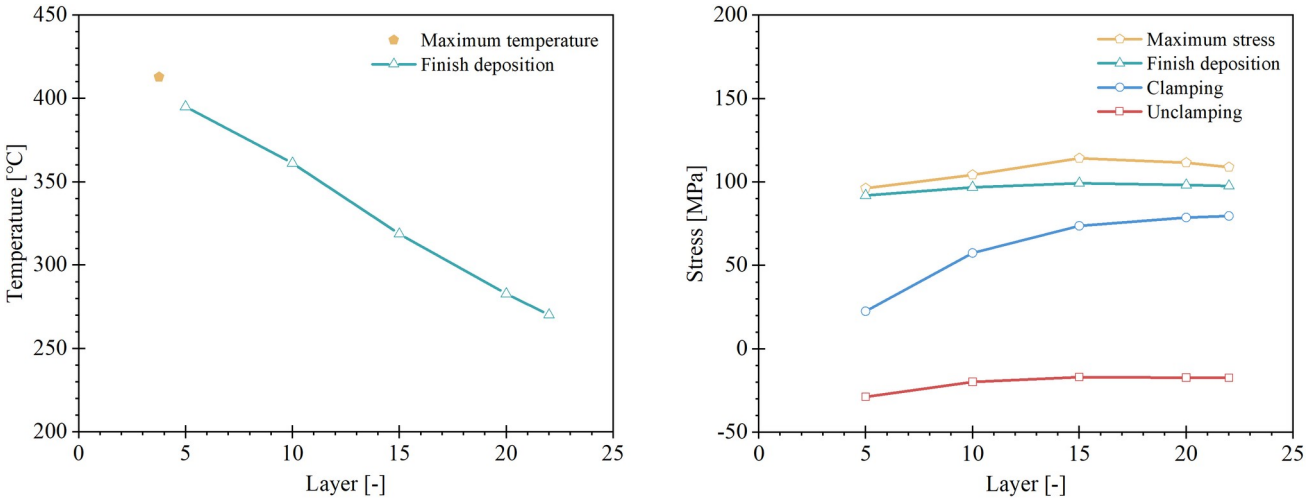


(a) Thermal trend of TC1 (b) Stress trend of SG

Fig. 22 Thermal and stress trends for specimens with varying deposition layers.

Fig. 23 illustrates the residual stresses along line EF in the unclamping and substrate removal stages. After unclamping, the longitudinal stresses in the final layer decrease significantly with more deposition layers, dropping from -17.6 MPa in the 5-layer specimen to -308.8 MPa in the 22-layer specimen. The transverse residual stress in the final layer initially decreases from the 5-layer specimen to the 15-layer specimen but then slightly increases in the 22-layer specimen. These variations result from the combined effects of increased system stiffness due to the larger volume of deposited material and the associated thermal deformation. Following substrate removal, the longitudinal residual stress follows a tension-compression pattern along the vertical profile of the specimen, with magnitudes significantly decreasing due to springback. For specimens with more than 5 layers, the transverse residual stresses exhibit a more complex zigzag pattern of alternating

tension and compression along line EF. Meanwhile, compared to longitudinal stresses, transverse residual stresses are less affected by substrate removal, as their overall shape and magnitude remain largely unchanged.

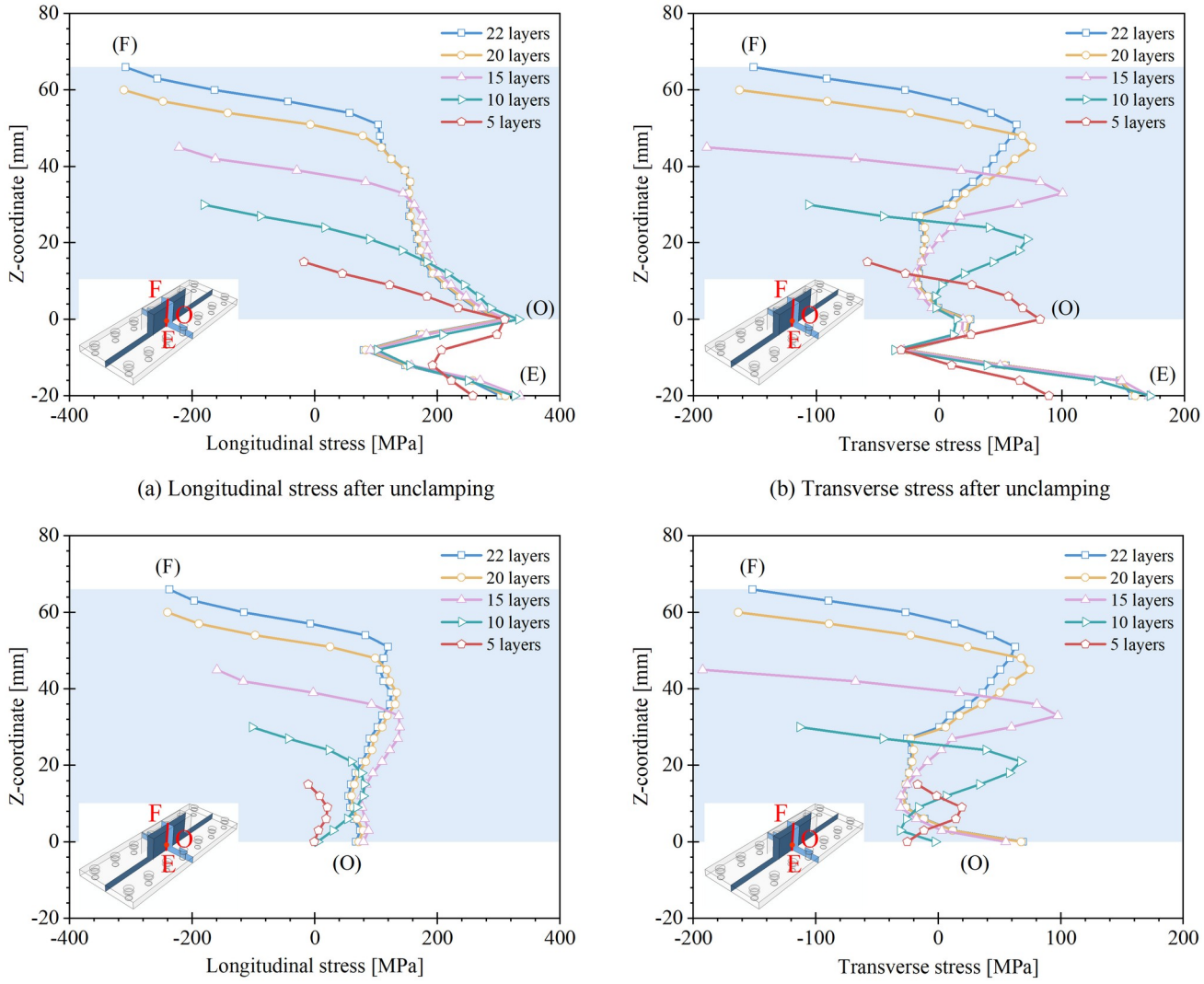


(a) Longitudinal stress after unclamping

(b) Transverse stress after unclamping

(c) Longitudinal stress after substrate removal

(b) Transverse stress after substrate removal

Fig. 23 Longitudinal and transverse residual stresses along EF with varying deposition layers.

## 5.3 Influence of platform conditions

The simulated thermal cycles and stress evolutions under different platform concepts were analysed. In Case 5 (without the platform), thermal cycles are comparable to those of Case 0, as similar thermal boundary conditions were applied. However, the increased flexibility of the boundary condition results in lower thermal stress. After unclamping, the residual stress amounts 4.7 MPa. In Case 6 (without bolts), the behaviour differs significantly. Lower temperatures are observed during the deposition stage, while higher temperatures occur during the cooling stage. This is attributed to the heat absorption effect of the thick substrate. The thick substrate in Case 6 also increases the

system stiffness, which reduces thermal stress compared to Case 0 during the process. However, after unclamping, the residual stress in Case 6 is -17.5 MPa, which is very close to the -17.4 MPa observed in Case 0. It is worth mentioning that Case 6 does not include bolts, and unclamping means removing the extended part of the substrate to restore the original thickness.

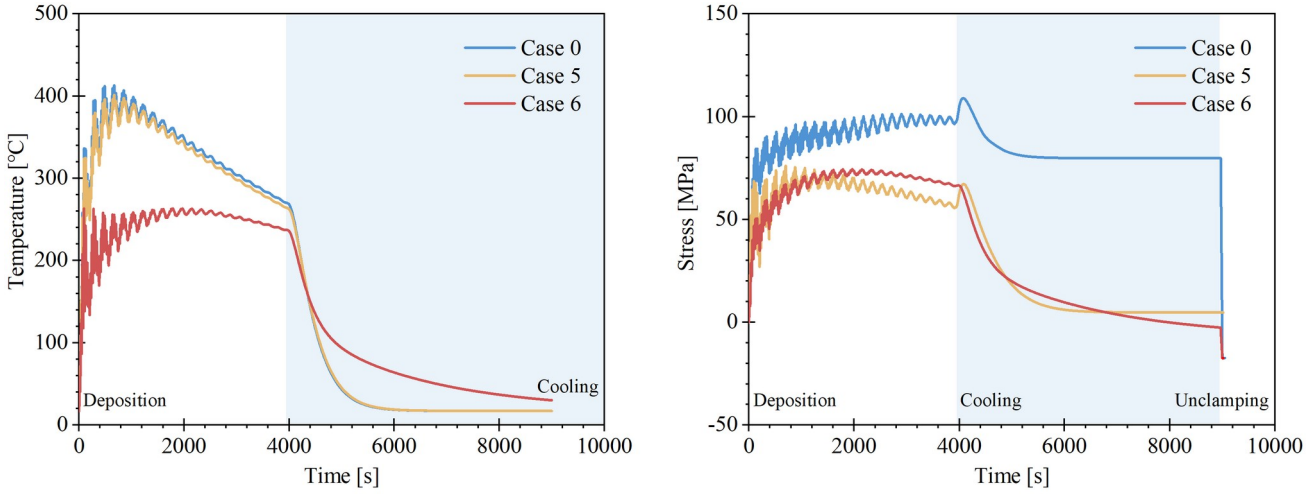


(a) Thermal cycles of TC1 (b) Stress evolutions of SG

Fig. 24 Simulated thermal cycles and stress evolutions under different boundary conditions.

The residual stress distributions for Case 5 and Case 6, both under clamping and after unclamping are shown in Fig. 25. After unclamping, the maximum von Mises stress is 487.7 MPa for Case 5 and 463.0 MPa for Case 6, compared to 517.3 MPa for Case 0. In Case 5, the high residual stress region spans a wide area of the substrate, reflecting the increased flexibility of the boundary condition without platform. This flexibility allows the stress to distribute more evenly across the substrate. In Case 6, the high residual stress is more concentrated around the connection between the substrate and the deposited wall. This is due to the increased stiffness introduced by the thick substrate, which restricts deformation and localizes the stress near the deposition-substrate interface.

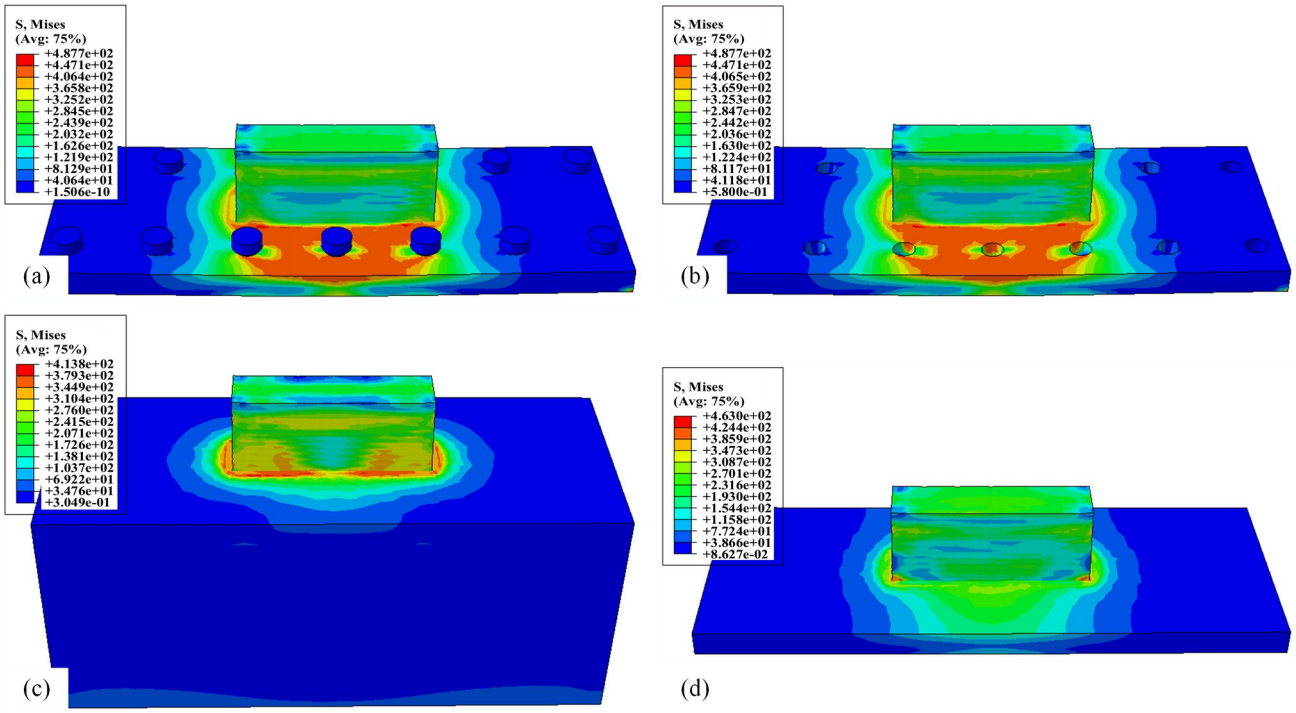


Fig. 25 Simulated residual stress distributions of: (a) Case 5 in clamping state; (b) Case 5 in unclamping state; (a) Case 6 in clamping state; (b) Case 6 in unclamping state.

The longitudinal and transverse stresses along line EF for different platform concepts are presented in Fig. 26. In terms of longitudinal stress, Case 5 has the highest tensile stress at the centre of the bottom substrate, reaching 473.7 MPa, while Case 6 shows the lowest value of 134.3 MPa. For transverse stress, Case 5 and Case 6 have values of 238.1 MPa and 181.3 MPa, respectively. Notably, stress distributions differ significantly in the lower deposited layers, whereas the upper layers follow a consistent trend. This suggests that the platform's influence on residual stresses is primarily concentred in the lower layers and diminishes with height. After substrate removal, the residual stress distributions for Case 0, Case 5, and Case 6 converge to similar patterns, indicating that the platform's impact on residual stresses is largely mitigated once the substrate is removed. As a result, the final residual stress magnitude and profiles become independent of the initial boundary conditions.

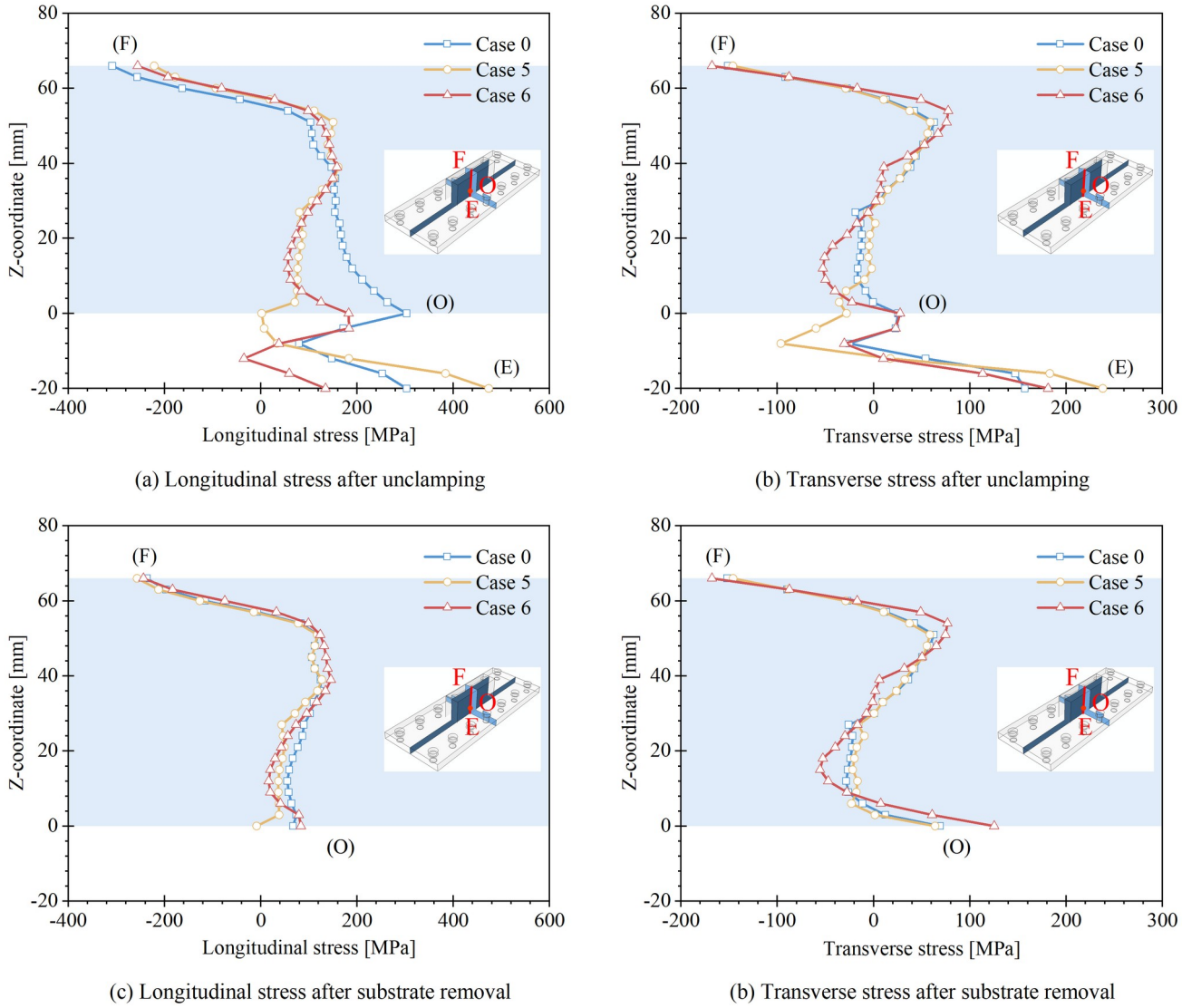


(a) Longitudinal stress after unclamping

(b) Transverse stress after unclamping

(c) Longitudinal stress after substrate removal

(b) Transverse stress after substrate removal

Fig. 26 Longitudinal and transverse stresses along line EF with different platforms.

## 6 Sensitivity assessment

WAAM is a complex process involving coupled thermal and stress phenomena, requiring careful consideration of multiple factors when modelling it with the FE method. To gain a deeper understanding of how various parameters affect simulation accuracy, sensitivity studies were performed on Case 2 (10 layers), balancing the need for stable temperature and stress predictions with computational efficiency. The following aspects were analysed: (1) Sequentially coupled thermal-stress analysis techniques; (2) Surface convection and radiation coefficients; (3) Heat source parameters; and (4) Bolt pretension force. These sensitivity studies provide insights into how specific modelling choices and parameter variations influence the accuracy and reliability of the FE simulations.

### 6.1 Sequentially coupled thermal-stress analysis

As discussed in Section 3, the validated approach employs a fully coupled three-dimensional thermal-mechanical model, which provides high accuracy but is computationally expensive. An alternative method sometimes used in FE simulation studies is the sequentially coupled model. In this approach, transient temperature evaluations are performed first, followed by mechanical analysis to calculate deformation and residual stress fields [64]. To assess the impact of computational techniques on the simulation results for the WAAM process, a sequentially coupled model was developed while keeping all other parameters unchanged. During the heat transfer simulation step, the deposited wall, bolts and substrate were modelled using DC3D8 solid elements, while the platform was meshed with DS4 shell elements. In the subsequent static general simulation step, C3D8R solid elements were used for the solid structures, and S4R shell elements were used for the platform.

Fig. 27 compares the numerical results of thermal cycles and stress evolutions for the fully coupled (FC) and sequentially coupled (SC) models. While the thermal cycles of both models follow the same overall trend, the SC model underestimates the temperatures. This discrepancy occurs because the SC model does not account for the effect of element deformation on the thermal field. At 670.8 s, the simulated peak temperature reached 412.9 ℃ for the FC model, and 309.9 ℃ for the SC model, compared to a measured temperature of 393.4 ℃. This corresponds to relative simulation errors of 5.0% for the FC model and 21.2% for the SC model. The SC model underestimates the temperature by 23.9% compared to the FC model. This underestimation also impacts stress predictions. During deposition, the SC model yields lower stress cycle amplitudes. At the fully cooled stage, the simulated residual stress is 76.5 MPa for the SC model, and 57.4 MPa for the FC model, with a relative difference of 33.3%. After unclamping, the SC model predicts a residual stress of -2.7 MPa, while the FC model gives -19.9 MPa, indicating a substantial discrepancy. The SC model's lower residual stress values are attributed to its reduced springback effect, a result of its simplified treatment of the interaction between thermal and mechanical fields.

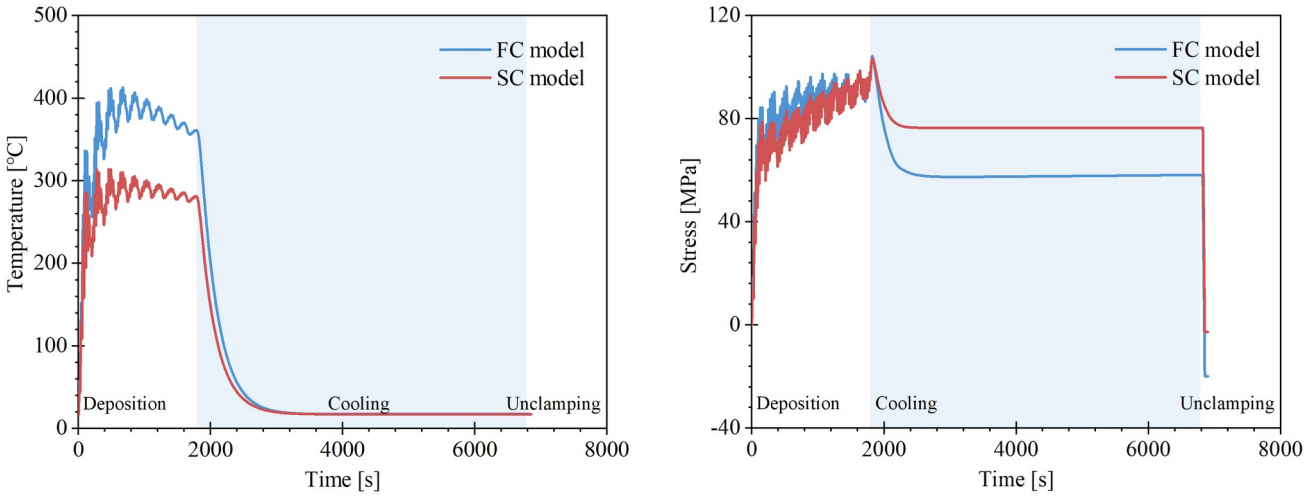


(a) Thermal cycles of TC1

(b) Stress evolutions of SG

Fig. 27 Comparison of thermal cycles and stress evolutions for FC and SC FE models.

The residual stress distributions simulated by FC and SC models along line EF are shown in Fig. 28. For longitudinal stresses, both the FC and SC models show a tension to compression stress pattern along line EF. However, the SC model underestimates the magnitude of longitudinal stresses compared to the FC model. For transverse residual stresses, the SC model fails to accurately predict the stress trends in the final few layers. Specifically, in the last layer, the SC model predicts a tensile stress of 55.9 MPa, whereas the FC model predicts a compressive stress of -106.5 MPa. After substrate removal, the SC model shows a different residual stress pattern compared to the FC model.

While the SC model underestimates temperature values and less accurately predicts residual stress distributions, it effectively captures the overall trends of temperature and stress evolutions. In terms of computational efficiency, the SC model achieved an 85.2% reduction in simulation time compared to the FC model. Given its significantly lower computational cost, the SC model remains a valuable tool for predicting WAAM processes, particularly when efficiency is prioritized over magnitude accuracy.

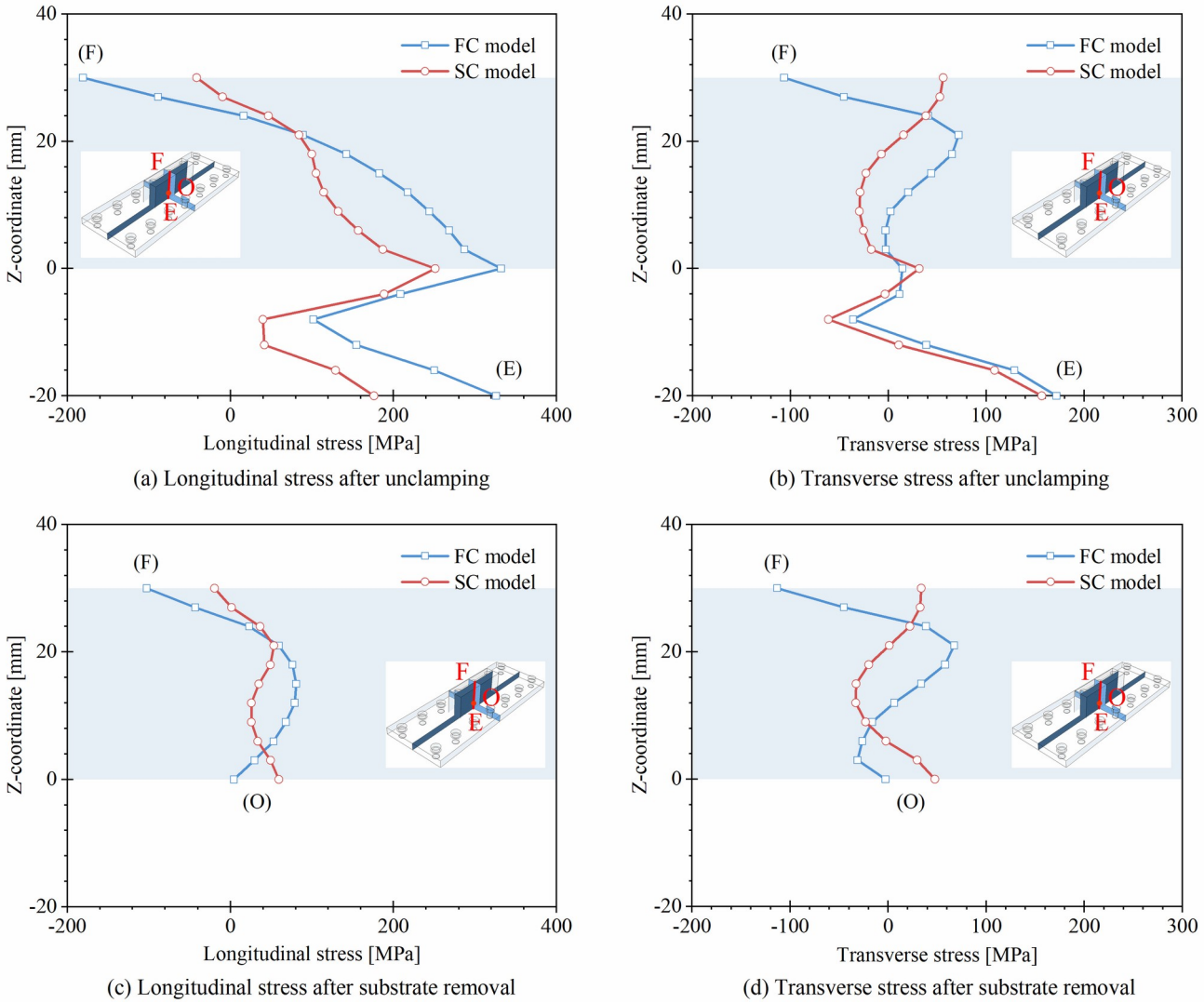


Fig. 28 Longitudinal and transverse stresses along line EF for FC and SC FE models.

## 6.2 Surface convection and radiation coefficients

Surface convection and radiation coefficients are critical in determining heat loss during the WAAM process, particularly as multiple layers of the specimen are deposited. These coefficients are influenced by several factors, including material chemical composition, temperature gradients, surface roughness, and the surrounding gas environment. However, there is a notable lack of consistent guidelines in the scientific literature for accurately defining these coefficients leading to significant variation in the values adopted by researchers, e.g. [65,66]. To investigate this, four groups of surface convection and radiation coefficients were selected based on values reported in previous studies on WAAM of steel [22,41,42], as summarised in Table 8. These groups were used to assess the sensitivity of the FE model to variations in these coefficients, providing insight into their impact on heat loss and residual stress distributions in WAAM simulations.

Table 8 Surface convection and radiation coefficients.

| FE model | CR1 | CR2 [22] | CR3 [41] | CR4 [42] |
|---|---|---|---|---|
| Radiation coefficient [-] | 0.73 | 0.2 | 0.5 | 0.5 |
| Top surface convection coefficient [W/(m$^2$K)] | 20 | 5.7 | 2.5 | 35 |
| Bottom surface convection coefficient [W/(m$^2$K)] | 300 | 300 | 2.5 | 2000 |

The simulated thermal cycles and stress evolutions under different surface convection and radiation coefficients (CR1 ~ CR4) are depicted in Fig. 29. These coefficients significantly affect both the thermal evolution and stress development during the WAAM process. The simulated peak temperatures at TC1 for CR1, CR2, CR3, and CR4 are 412.9 ℃, 468.4 ℃, 814.8 ℃ and 278.0 ℃, respectively. The corresponding residual stresses at SG after unclamping are -19.9 MPa, -27.2 MPa, -48.5 MPa, and -11.1 MPa. The results confirm that higher surface convection and radiation coefficients result in greater heat loss, reducing the simulated thermal cycles while increasing the residual stresses in the specimen. This analysis highlights the role of rapid cooling and heat dissipation in stress development.

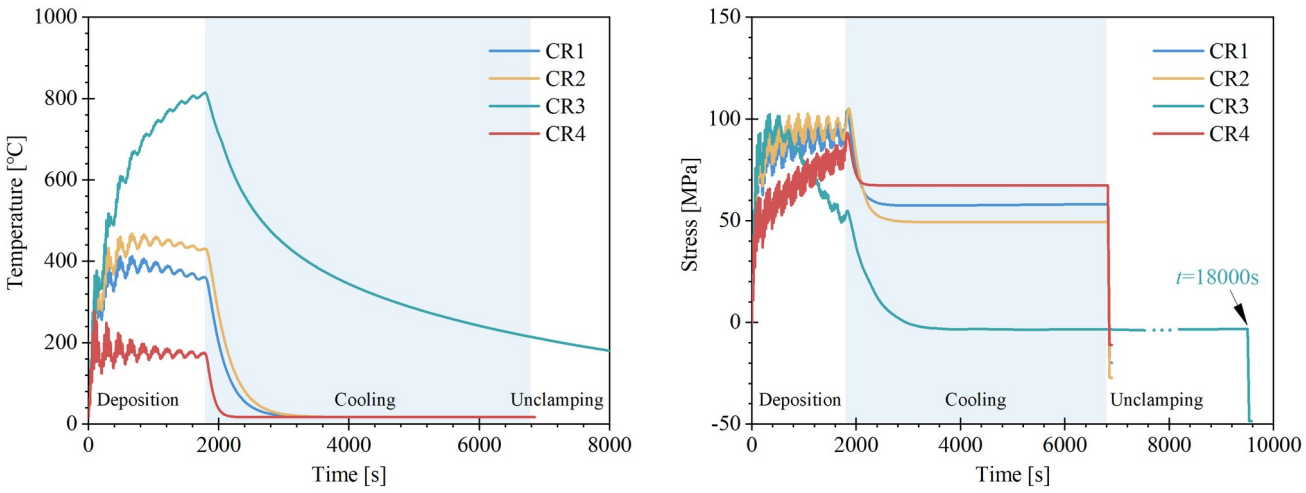


(a) Thermal cycles of TC1 (b) Stress evolutions of SG

Fig. 29 Comparison of thermal cycles and stress evolutions under different surface convection and radiation

Fig. 30 presents the residual stress distributions along line EF after unclamping and substrate removal. For longitudinal residual stresses, different surface convection and radiation coefficients results in similar trends, with a consistent stress evolution across the vertical profile of the specimen. In contrast, the transverse residual stress patterns vary significantly across the different coefficient groups, demonstrating the higher sensitivity of transverse stresses to changes in heat dissipation. This analysis reinforces the critical importance of accurately selecting surface convection and radiation coefficients, as these parameters directly affect the temperature field and, consequently, the residual

stress distributions. Proper calibration of these coefficients is essential to improving the predictive accuracy of FE simulations for WAAM processes.

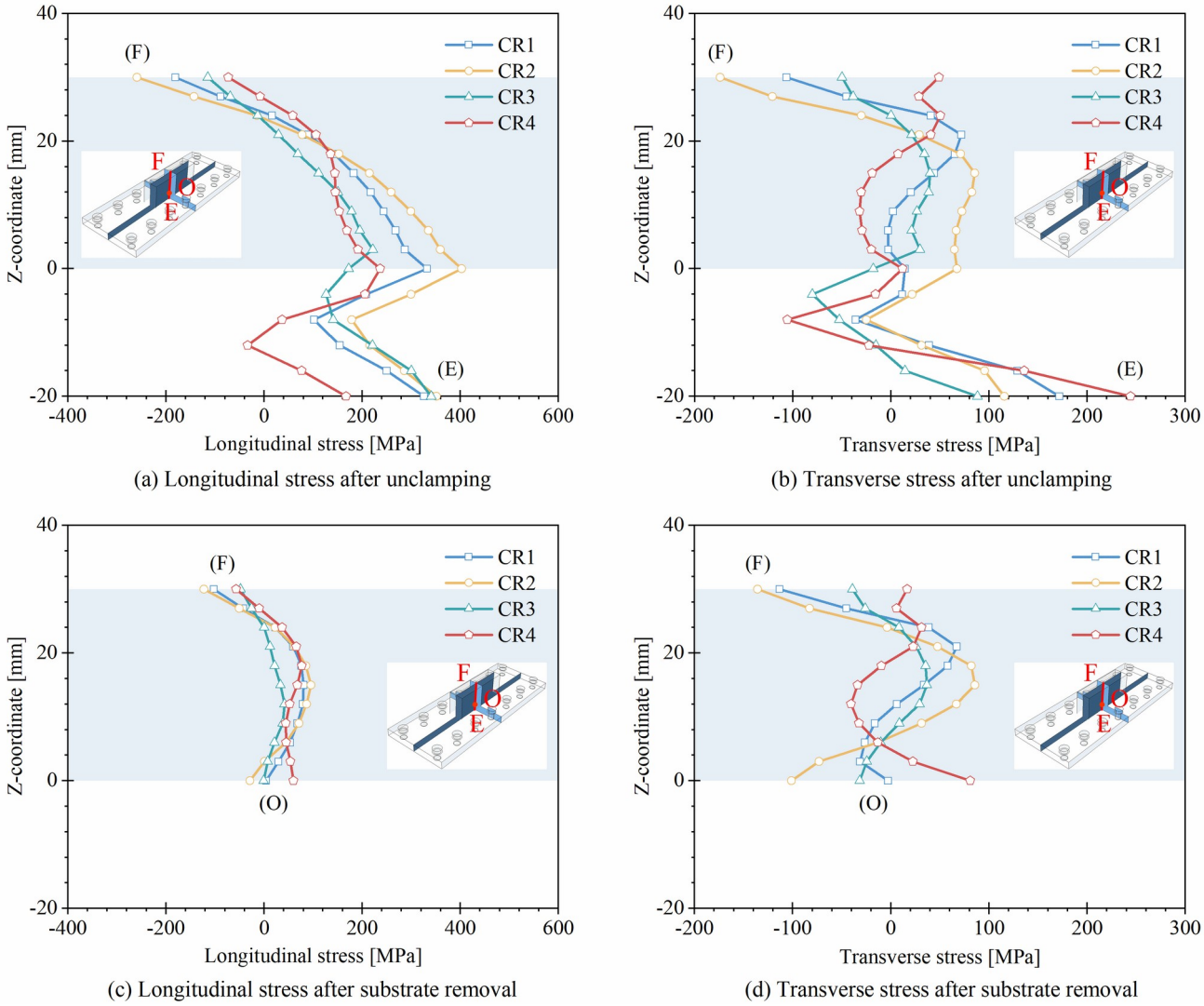


Fig. 30 Longitudinal and transverse stresses along line EF with different surface convection and radiation coefficients.

## 6.3 Heat source parameters

The shape of the molten pool is highly sensitive to predefined heat source parameters, as they directly influence the temperature field and stress distribution during the WAAM process. Various heat source models have been proposed, including the normal distribution model [67] and the equivalent heat source model [27]. Their mathematical expressions, describing the spatial and temporal characteristics of heat input, are provided in Equations (15) and (16).

Normal distribution model

$$Q(x,y,t)=\frac{3\eta P}{ab\pi}\exp\left(\frac{-3(x-vt)^2}{a^2}-\frac{3y^2}{b^2}\right) \tag{15}$$

Equivalent heat source

$$Q(x,y,z,t)=\frac{\eta P}{wlh} \tag{16}$$

The normal distribution surface model assumes a Gaussian heat distribution, where parameters *a* and *b* define the major and minor axes of the elliptical heat distribution respectively. Heat is applied to the top surface of the newly deposited layer. The equivalent heat source model simplifies the heat source geometry and distribution by uniformly applying heat to the activated elements during the activation step. Parameters *w*, *l*, and *h* represent the width, total length of the activated elements, and layer thickness respectively. The parameter values for these two heat source models, along with the double ellipsoidal heat source used in Sections 3 and 4, are listed in Table 9. Compared to the double ellipsoidal heat source (HS1), HS2 and HS3 offer greater simplicity and ease of implementation but may result in higher simulation errors.

Table 9 Heat source parameter values.

| FE model | Heat source model | Parameter values |
|---|---|---|
| HS1 | Double ellipsoidal heat source | $a_f$ = 4.0, $a_r$ = 11.0, $b$ = 3.6, $c$ = 4.0, $f_f$ = 0.6, $f_r$ = 1.4, $\eta$ = 0.9 |
| HS2 | Normal distribution model | $a$ = 4.0, $b$ = 3.6, $\eta$ = 0.9 |
| HS3 | Equivalent heat source | $w$ = 3.4, $l_1$ = 24.5 / $l_2$ = 28, $h$ = 3.0, $\eta$ = 0.9 |

The simulated temperature cycles and stress evolutions for different heat source models are shown in Fig. 31. The maximum simulated temperatures at TC1 are 412.9 ℃, 282.9 ℃, and 461.0 ℃ for HS1, HS2 and HS3, respectively. The corresponding residual stresses at SG after unclamping are -19.9 MPa, -1.6 MPa and -28.6 MPa. The results show that the overall temperature and stress fields are highly sensitive to the choice of heat source models. For HS2, the heat energy is applied to the top surface of the current deposition layer, generating extremely high surface temperatures. These elevated surface temperatures result in increased heat losses. HS3 produces more balanced thermal behaviour, as the heat is uniformly applied to the nodes of the newly deposited material. These heat source models also generate varying energy densities at the FE model's nodes, causing differences in heat energy absorption. As a result, the actual energy introduced into the computational domain can differ significantly between models, leading to distinct temperature and residual stress outcomes.

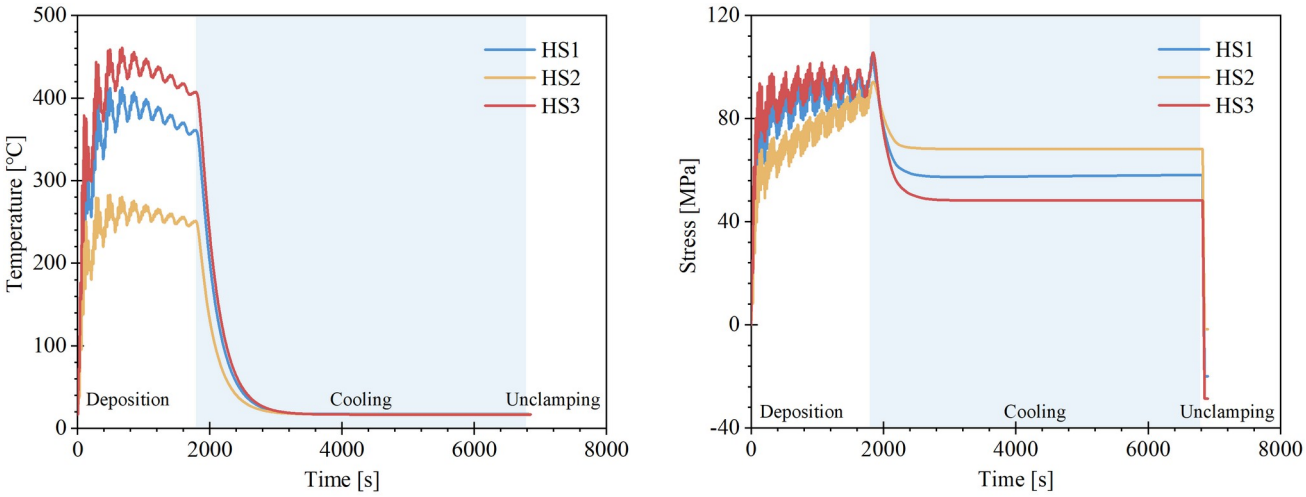


(a) Thermal cycles of TC1

(b) Stress evolutions of SG

Fig. 31 Comparison of thermal cycles and stress evolutions for different heat source models.

The simulated residual stresses along line EF for different heat sources are shown in Fig. 32. Consistent with the findings in Sections 6.1 and 6.2, lower thermal cycles (as in HS2) result in a reduced magnitude of longitudinal residual stress. Additionally, HS2 fails to capture the compressive transverse residual stress within the final few layers due to its lower heat input. The residual stress patterns obtained using HS2 after unclamping and substrate removal are comparable to those obtained from the SC model. This similarity arises because both HS2 and SC models underestimate temperature evolutions, leading to reduced accuracy in predicting stress distributions. For HS3, the higher temperatures result in residual stress patterns similar to those of HS1, but with different magnitudes. The elevated temperatures in HS3 cause greater thermal expansion and relaxation effects, which influence the overall stress distribution.

These findings emphasise the importance of conducting heat source parameter calibrations as it was done in the present study. Proper calibration ensures that the heat source accurately represents the physical process, allowing the model to replicate the thermal, stress and deformation behaviours observed during the actual WAAM process.

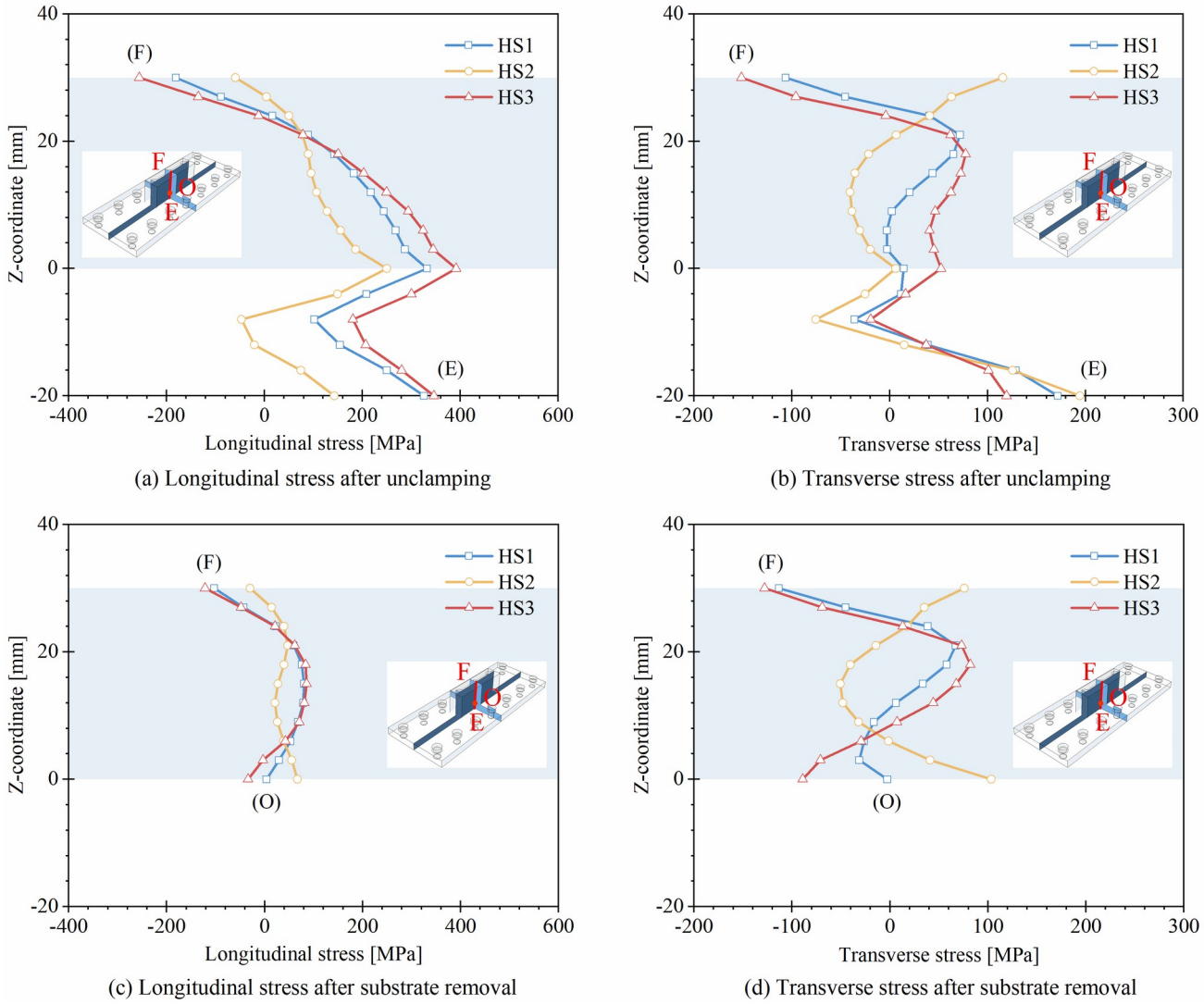


Fig. 32 Longitudinal and transverse stresses along line EF for different heat source models.

## 6.4 Bolt pretension force

Neglecting bolt pretensions in WAAM process simulations can greatly simplify FE models, as demonstrated in studies such as [16,25,68]. However, it has been observed that stress distribution in the substrate is highly sensitive to bolt pretension forces (i.e. stiffness). Ignoring bolt preload effects can lead to significant deviations in the simulated stress field, as highlighted in [8]. In this study, the pretension force applied to the bolts was 10.2 kN. To further investigate the impact of bolt pretensions on stress distribution, FE simulations were performed using five different preload force levels: 0 kN, 10.2 kN, 20.4 kN, 34.0 kN, and 54.5 kN. These force levels were selected based on typical pretension values provided in [69], as summarised in Table 9.

Table 10 Selected bolt pretension force levels.

| FE model | PF1 | PF2 | PF3 | PF4 | PF5 |
|---|---|---|---|---|---|
| Pretension force (kN) | 0 | 10.2 | 20.4 | 34.0 | 54.5 |

The thermal cycles are insensitive to changes in bolt pretension forces, as the thermal profiles for all cases (PF1 ~ PF5) overlap, i.e., the same as 10-layer curve in Fig. 21(a). The stress evolutions and trends for different bolt pretension forces are presented in Fig. 33. PF1 (no pretension force) exhibits the lowest stress values during the deposition and cooling stages. As the pretension force increases, stresses rise and eventually converge when preloads reach 34.0 kN and 54.5 kN. This convergence occurs because excessive system stiffness restricts further development of stress, even though moderate stiffness initially increases stress evolution. After unclamping, the residual stresses are similar across all cases.

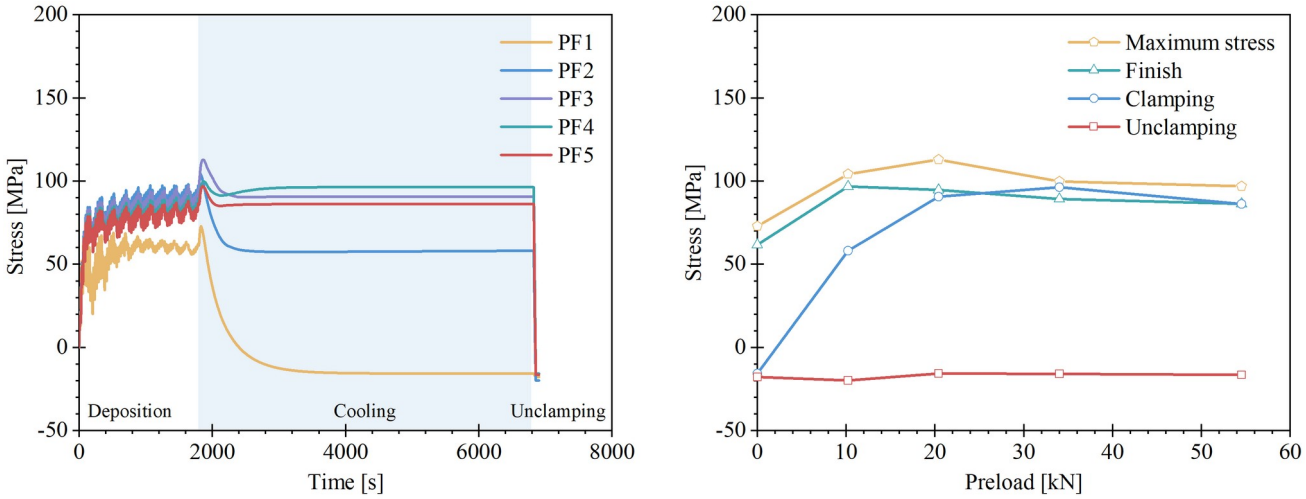


(a) Stress evolutions of SG

(b) Stress trends of SG

Fig. 33 Stress evolutions and trends for different bolt pretension forces.

The simulated residual stress distributions along line EF are shown in Fig. 34. The overall residual stress patterns for different pretension forces follow a similar trend. For longitudinal residual stress after unclamping, a consistent pattern is observed across all cases: the stress transitions from tensile at the bottom of the substrate to compressive in the top layers of the deposited wall. For transverse stress, the patterns vary slightly depending on the pretension forces: PF1 shows a more complex transverse stress evolution compared to PF5 which exhibits a simplified transverse stress evolution.

These results demonstrate that bolt pretension forces significantly impact stress evolution during the deposition and cooling stages. However, their influence on residual stresses is partially mitigated after unclamping, as the system undergoes springback and stress redistribution. It is important to account for bolt pretension forces when predicting stress behaviour during the

intermediate stages of the WAAM process. Nevertheless, their influence is largely removed after unclamping and substrate removal, resulting in consistent overall stress distribution trends across different pretension levels.

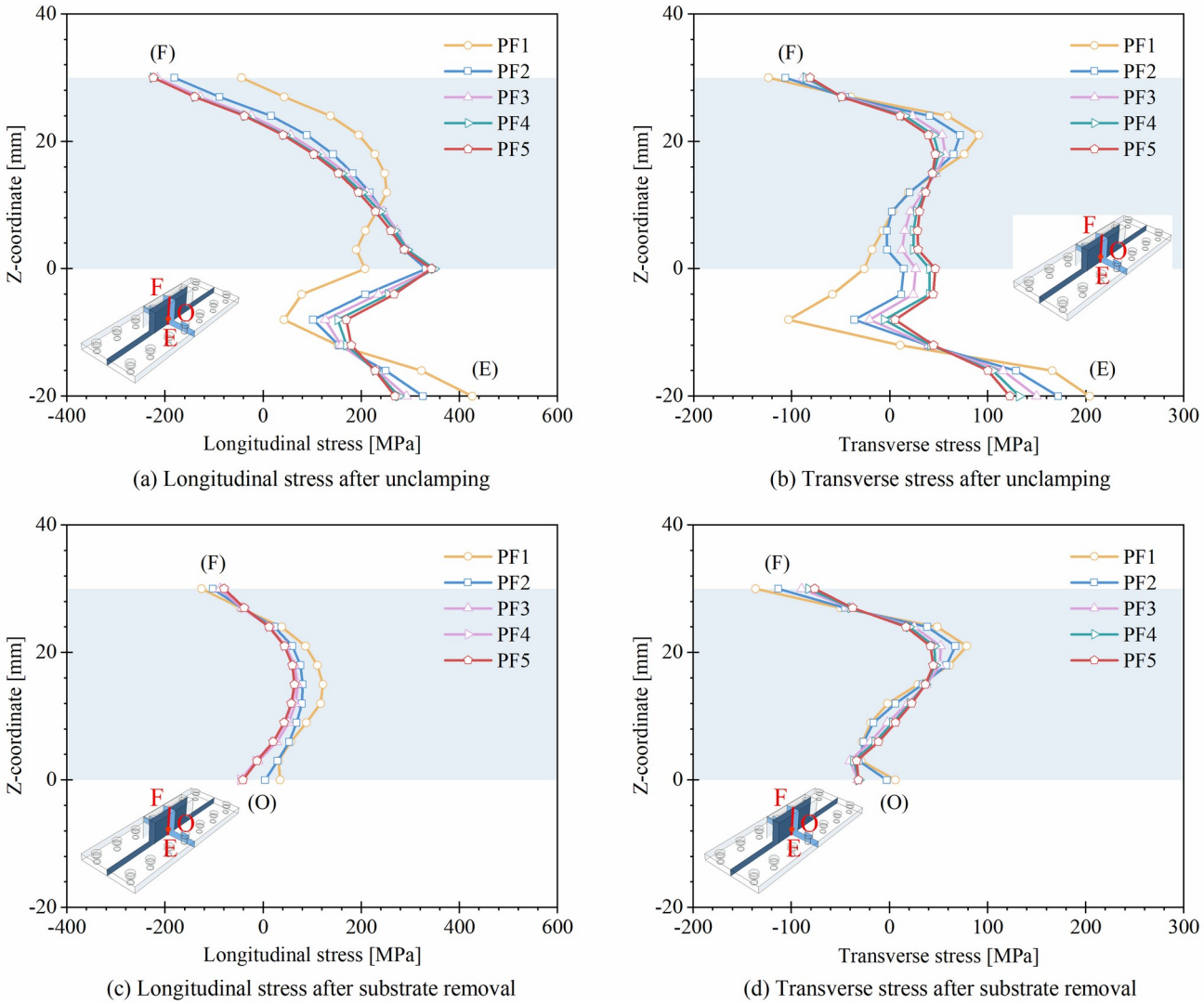


(a) Longitudinal stress after unclamping

(b) Transverse stress after unclamping

(c) Longitudinal stress after substrate removal

(d) Transverse stress after substrate removal

Fig. 34 Longitudinal and transverse stresses along line EF for different bolt pretension forces.

## 7 Conclusions and recommendations

This paper investigates the temperature and stress development occurring during the wire arc additive manufacturing (WAAM) process via the finite element (FE) model. It provides an in-depth analysis of temperature evolution, strain variations, and residual stress distribution across the deposition process, with rigorous validation against measurements of temperatures and stresses during the process. Residual stresses in specimens with varying numbers of deposited layers and boundary conditions are analysed, along with a sensitivity assessment of key FE model parameters. Based on these findings, we produced longitudinal and transverse residual stress patterns normalised

by the yield strength $f_y$ = 308.4 MPa, across the specimen's height, see Table 11 where the key model parameters are summarised.

Additionally, the following conclusions can be drawn:

(1) The proposed three-dimensional coupled thermal and mechanical FE model with its hypotheses on the physical and mechanical material properties and the heat source model accurately simulates temperature and stress development during the WAAM of 3Dprint AM35 components (S355 grade).

(2) The sequentially coupled FE model enables faster computation but underestimates temperature values and is less accurate in predicting residual stress distributions compared to the fully coupled FE model. However, it effectively captures overall trends in temperature and stress evolutions.

(3) Conducting heat source parameter calibrations and mesh sensitivity analyses is critical for accurate FE simulations. Proper calibration ensures that the heat source accurately represents the physical process, replicating the observed thermal and stress behaviours.

(4) Boundary conditions (i.e., the presence of substrate constraints and bolt pretension forces) have a significant impact on residual stress distributions during deposition and cooling due to increased system stiffness, hence restricted deformation. However, their influence within the deposited specimen is largely mitigated by removing the substrate.

(5) Residual stress patterns are mostly influenced by the number of deposited layers. The interaction between deformation and system stiffness, varying with the number of deposited layers, plays a key role in shaping the evolution of residual stress distributions.

(6) Longitudinal residual stresses show similar trends across different surface convection and radiation coefficient groups, while transverse residual stress patterns show significant variations, highlighting the sensitivity of transverse stresses to heat dissipation parameters.

In summary, to ensure the accuracy of numerical residual stress predictions in WAAM, we recommend adopting a fully coupled FE model, calibrating double ellipsoidal heat source parameters

based on single-pass deposition tests conducted under identical process parameters, accounting for bolt pretension effects, and maintaining consistent boundary concepts.

The influence of cross-sectional geometries within a single deposition layer will be investigated in the future to study their influence on residual stress distribution. Meanwhile, future research will also integrate advanced optimization techniques, such as topology optimization, with metal additive manufacturing to enhance design flexibility, improve performance, and enable functional integration in engineering applications [70,71].

Table 11 Residual stress patterns (normalised by the yield strength $f_y$ = 308.4 MPa) across the specimen's height with key model parameters.

| Model parameters | Parameter values | Residual stress patterns along heights |
|---|---|---|
| Deposition layer | • 5 layers<br>• 10 layers<br>• 15 layers<br>• 20 layers<br>• 22 layers | 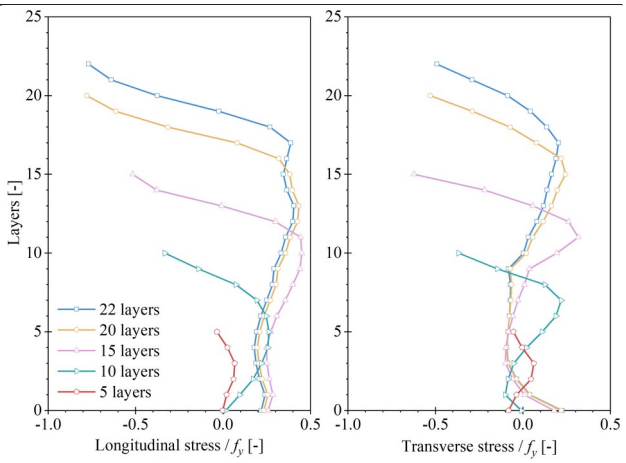 |
| Platform concepts (22 layers) | • Boundary with platform and bolts<br>• Boundary without platform<br>• Boundary without bolts | 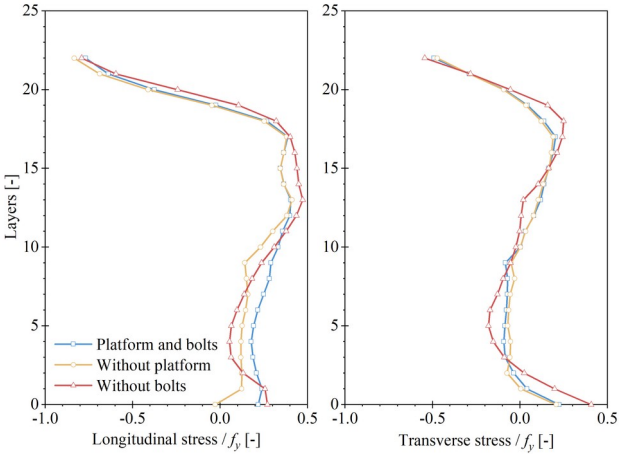 |

| | | |
|---|---|---|
| Bolt pretension force (10 layers) | • 0 kN<br>• 10.2 kN<br>• 20.4 kN<br>• 34.0 kN<br>• 54.5 kN | 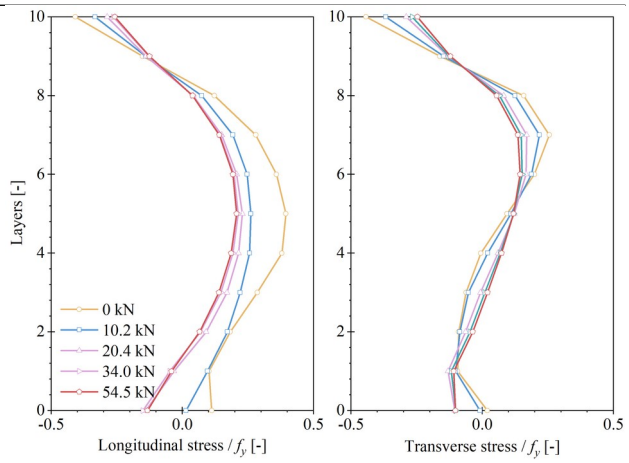 |
| Analysis techniques (10 layers) | • Fully coupled (FC) thermal-mechanical analysis<br>• Sequentially coupled (SC) thermal-mechanical analysis | 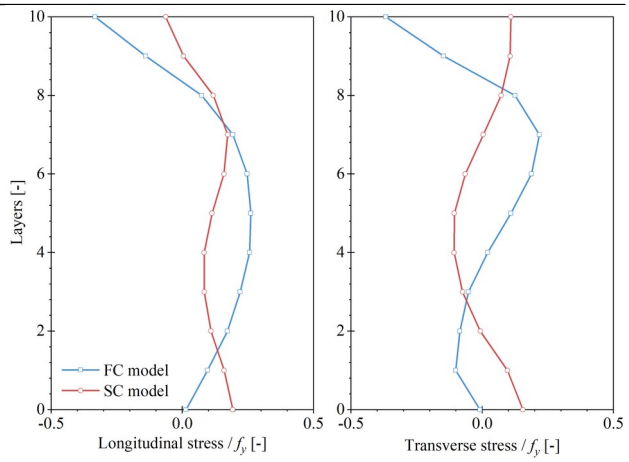 |
| Surface convection and radiation coefficients (10 layers) | • CR1: $\varepsilon = 0.73$, $h_1 = 20\,W/(m^2K)$, $h_2 = 300\,W/(m^2K)$<br>• CR2: $\varepsilon = 0.2$, $h_1 = 5.7\,W/(m^2K)$, $h_2 = 300\,W/(m^2K)$<br>• CR3: $\varepsilon = 0.5$, $h_1 = 2.5\,W/(m^2K)$, $h_2 = 2.5\,W/(m^2K)$<br>• CR4: $\varepsilon = 0.5$, $h_1 = 35\,W/(m^2K)$, $h_2 = 2000\,W/(m^2K)$ | 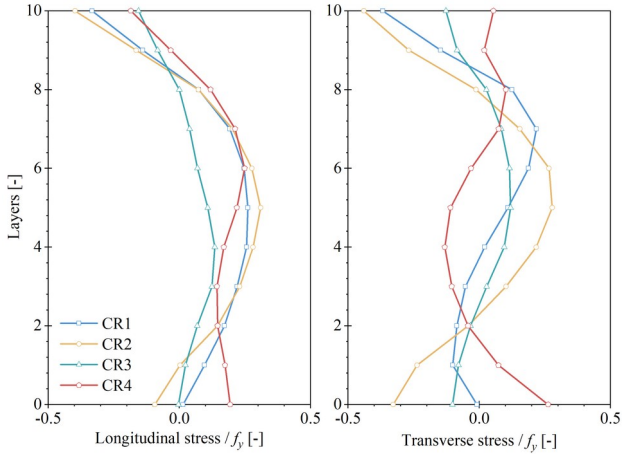 |
| Heat source parameters (10 layers) | • HS1: Double ellipsoidal heat source<br>• HS2: Normal distribution heat source<br>• HS3: Equivalent heat source | 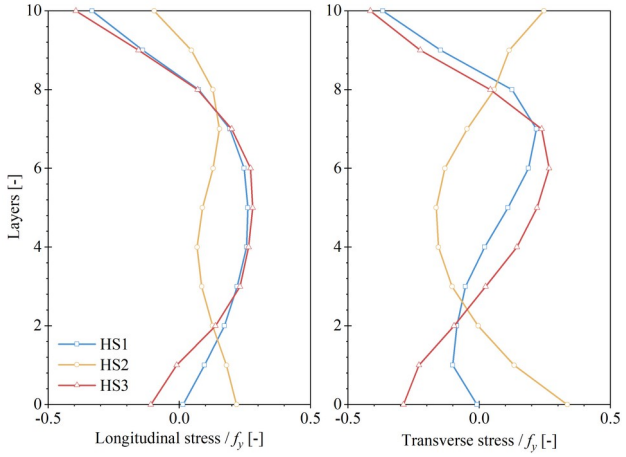 |

1

1

## Appendix

A mesh convergence study was conducted in [8] to evaluate the sensitivity of simulation accuracy to different FE mesh sizes of 1 mm, 2 mm, and 3 mm. As shown in Fig. A.1, the thermal cycles and stress development predicted using the three mesh sizes were compared against experimental measurements. All models reproduced the thermal and mechanical responses with reasonable accuracy. For temperature predictions, the measured peak temperature was 173.2 °C, with relative simulation errors of 6.3%, 7.7%, and 10.7% for the 1 mm, 2 mm, and 3 mm meshes, respectively. For stress predictions, the first peak stress was 117.6 MPa, with deviations of 7.0%, 16.2%, and 21.3%, respectively. Although the 1 mm mesh provided the highest accuracy, it required approximately twelve times more computational time than the 3 mm mesh, while offering only marginal improvements in accuracy. Therefore, to achieve an optimal balance between computational cost and simulation fidelity, a 3 mm mesh was adopted in this study.

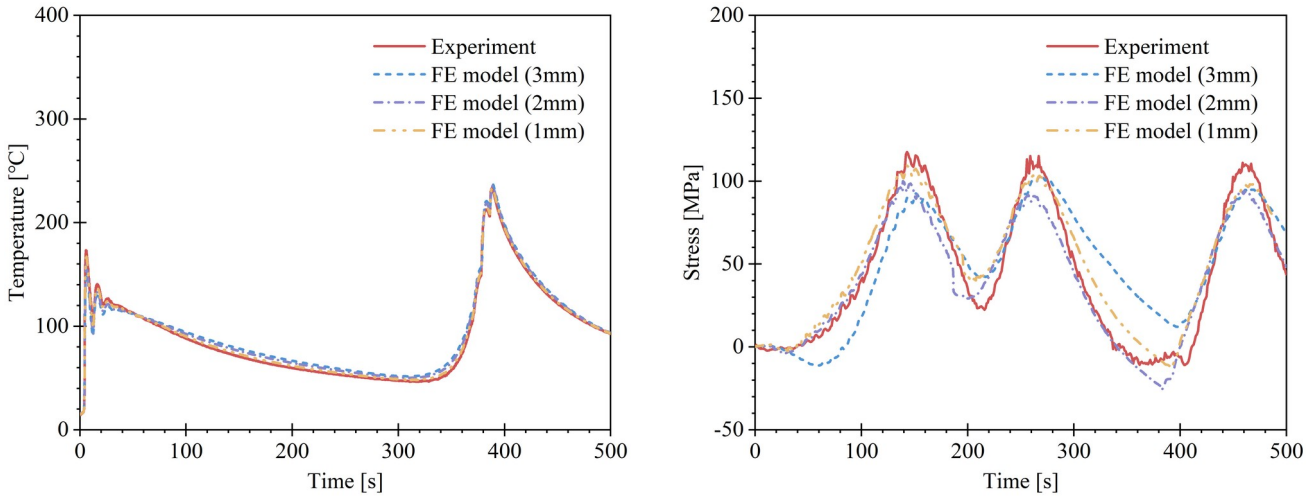


Fig. A.135 Comparison of simulated thermal cycles and stress evolutions for mesh sizes of 1 mm, 2 mm, and 3 mm, adopted from [8].


## Acknowledgements

We would also like to warmly thank Ken Whittaker and Scott MacDonald of Whittaker Engineering for their unrelenting dedication to the accomplishment of our experiments.

# References


[1] Karunakaran KP, Suryakumar S, Pushpa V, Akula S. Low cost integration of additive and subtractive processes for hybrid layered manufacturing. Robot Comput Integr Manuf 2010;26:490–9. https://doi.org/10.1016/j.rcim.2010.03.008.

[2] Song YA, Park S. Experimental investigations into rapid prototyping of composites by novel hybrid deposition process. J Mater Process Technol 2006;171:35–40. https://doi.org/10.1016/j.jmatprotec.2005.06.062.

[3] Bhakthavatchalam U, Ganeshmurthy K, Jaisooriyan A. Additive Manufacturing Using MIG Welding. International Journal of Research in Engineering, Science and Management 2018;1.

[4] Ruan X, Karabulut B, Dobri J, Rossi B. Generalised notch stress method to evaluate the fatigue behaviour of rough and smooth wire arc additively manufactured components 2025;199. https://doi.org/10.1016/j.ijfatigue.2025.109045.

[5] Chen Y, Chen MT, Zhao O, Rossi B, Ruan X. Fatigue crack growth behavior of wire arc additively manufactured 316L austenitic stainless steel. Thin-Walled Structures 2025;212:113182. https://doi.org/10.1016/j.tws.2025.113182.

[6] Wang Z, Hou Y, Huang C, Han Q, Zong L, Chen M-T, et al. Experimental study and constitutive modelling of wire arc additively manufactured steel under cyclic loading. J Constr Steel Res 2024;213:108420. https://doi.org/10.1016/j.jcsr.2023.108420.

[7] Karabulut B, Ruan X, MacDonald S, Dobrić J, Rossi B. Fatigue of wire arc additively manufactured components made of unalloyed S355 steel. Int J Fatigue 2024;184. https://doi.org/10.1016/j.ijfatigue.2024.108317.

[8] Ruan X, Karabulut B, MacDonald S, Dobrić J, Rossi B. Effect of boundary conditions on residual stress in cold metal transfer-based wire arc additively manufactured steel components. Mater Des 2025;249. https://doi.org/10.1016/j.matdes.2024.113548.

[9] Chen MT, Chen Y, Huang C, Gardner L, Zhao O. Experimental investigation of fatigue crack growth in wire arc additively manufactured ER2209 duplex stainless steel. J Constr Steel Res 2025;231:109615. https://doi.org/10.1016/j.jcsr.2025.109615.

[10] Huang C, Kyvelou P, Gardner L. Stress-strain curves for wire arc additively manufactured steels. Eng Struct 2023;279:115628. https://doi.org/10.1016/j.engstruct.2023.115628.

[11] Huang C, Hadjipantelis N, Quan S, Chen T, Gardner L. Mechanical properties of wire arc additively manufactured steels at polar temperatures. Structures 2024;70:107627. https://doi.org/10.1016/j.istruc.2024.107627.

[12] Lindgren LE. Numerical modelling of welding. Comput Methods Appl Mech Eng 2006;195:6710–36. https://doi.org/10.1016/j.cma.2005.08.018.

[13] Srivastava S, Garg RK, Sharma VS, Sachdeva A. Measurement and Mitigation of Residual Stress in Wire-Arc Additive Manufacturing: A Review of Macro-Scale Continuum Modelling Approach. Archives of Computational Methods in Engineering 2021;28:3491–515. https://doi.org/10.1007/s11831-020-09511-4.

[14] Bayat M, Dong W, Thorborg J, To AC, Hattel JH. A review of multi-scale and multi-physics simulations of metal additive manufacturing processes with focus on modeling strategies. Addit Manuf 2021;47:102278. https://doi.org/10.1016/j.addma.2021.102278.

[15] Barath Kumar MD, Manikandan M. Assessment of Process, Parameters, Residual Stress Mitigation, Post Treatments and Finite Element Analysis Simulations of Wire Arc Additive Manufacturing Technique. Metals and Materials International 2022;28:54–111. https://doi.org/10.1007/S12540-021-01015-5.

[16] Escribano-García R, Rodriguez N, Zubiri O, Piccini J, Setien I. 3D numerical simulation of GMAW Cold Metal Transfer using response surface methodology. J Manuf Process 2022;76:656–65. https://doi.org/10.1016/j.jmapro.2022.02.043.

[17] Somashekara MA, Naveenkumar M, Kumar A, Viswanath C, Simhambhatla S. Investigations into effect of weld-deposition pattern on residual stress evolution for metallic additive manufacturing. International Journal of Advanced Manufacturing Technology 2017;90:2009–25. https://doi.org/10.1007/S00170-016-9510-7/METRICS.

[18] Ling Y, Ni J, Antonissen J, Ben Hamouda H, Vande Voorde J, Abdel Wahab M. Numerical prediction of microstructure and hardness for low carbon steel wire Arc additive manufacturing components. Simul Model Pract Theory 2023;122. https://doi.org/10.1016/j.simpat.2022.102664.

[19] Cadiou S, Courtois M, Carin M, Berckmans W, Le Masson P. Heat transfer, fluid flow and electromagnetic model of droplets generation and melt pool behaviour for wire arc additive manufacturing. Int J Heat Mass Transf 2020;148:119102. https://doi.org/10.1016/J.IJHEATMASSTRANSFER.2019.119102.

[20] Li Y, Yun Z, Zhang W, Long X, Zhu J. 3D Modelling of Layer-by-Layer Heat and Mass Transfer in Wire Arc Additive Manufacturing. Additive Manufacturing Frontiers 2024;3:200159. https://doi.org/10.1016/J.AMF.2024.200159.

[21] Xiong Y, Dharmawan AG, Tang Y, Foong S, Soh GS, Rosen DW. A knowledge-based process planning framework for wire arc additive manufacturing. Advanced Engineering Informatics 2020;45:101135. https://doi.org/10.1016/J.AEI.2020.101135.

[22] Ding J, Colegrove P, Mehnen J, Ganguly S, Almeida PMS, Wang F, et al. Thermo-mechanical analysis of Wire and Arc Additive Layer Manufacturing process on large multi-layer parts. Comput Mater Sci 2011;50:3315–22. https://doi.org/10.1016/j.commatsci.2011.06.023.

[23] Nguyen L, Buhl J, Israr R, Bambach M. Analysis and compensation of shrinkage and distortion in wire-arc additive manufacturing of thin-walled curved hollow sections. Addit Manuf 2021;47:102365. https://doi.org/10.1016/j.addma.2021.102365.

[24] Deng D, Murakawa H. Numerical simulation of temperature field and residual stress in multi-pass welds in stainless steel pipe and comparison with experimental measurements. Comput Mater Sci 2006;37:269–77. https://doi.org/10.1016/j.commatsci.2005.07.007.

[25] Li R, Xiong J, Lei Y. Investigation on thermal stress evolution induced by wire and arc additive manufacturing for circular thin-walled parts. J Manuf Process 2019;40:59–67. https://doi.org/10.1016/j.jmapro.2019.03.006.

[26] Li R, Wang G, Zhao X, Dai F, Huang C, Zhang M, et al. Effect of path strategy on residual stress and distortion in laser and cold metal transfer hybrid additive manufacturing. Addit Manuf 2021;46:102203. https://doi.org/10.1016/j.addma.2021.102203.

[27] Dong W, Jimenez XA, To AC. Temperature-dependent modified inherent strain method for predicting residual stress and distortion of Ti6Al4V walls manufactured by wire-arc directed energy deposition. Addit Manuf 2023;62:103386. https://doi.org/10.1016/j.addma.2022.103386.

[28] Geng R, Du J, Wei Z, Ma N. Multiscale modelling of microstructure, micro-segregation, and local mechanical properties of Al-Cu alloys in wire and arc additive manufacturing. Addit Manuf 2020;36:101735. https://doi.org/10.1016/j.addma.2020.101735.

[29] Huang J, Li Z, Yu S, Yu X, Fan D. Real-time observation and numerical simulation of the molten pool flow and mass transfer behavior during wire arc additive manufacturing. Welding in the World 2022;66:481–94. https://doi.org/10.1007/S40194-021-01214-Z/FIGURES/13.

[30] Bai X, Colegrove P, Ding J, Zhou X, Diao C, Bridgeman P, et al. Numerical analysis of heat transfer and fluid flow in multilayer deposition of PAW-based wire and arc additive manufacturing. Int J Heat Mass Transf 2018;124:504–16. https://doi.org/10.1016/J.IJHEATMASSTRANSFER.2018.03.085.

[31] Kyvelou P, Spinasa A, Gardner L. Testing and analysis of optimised wire arc additively manufactured steel trusses. Ce/Papers 2023;6:726–31. https://doi.org/10.1002/cepa.2500.

[32] Ravisankar A, Velaga SK, Rajput G, Venugopal S. Influence of welding speed and power on residual stress during gas tungsten arc welding (GTAW) of thin sections with constant heat input: A study using numerical simulation and experimental validation. J Manuf Process 2014;16:200–11. https://doi.org/10.1016/j.jmapro.2013.11.002.

[33] Pramod R, Mohan Kumar S, Girinath B, Rajesh Kannanc A, Pravin Kumar N, Siva Shanmugam N. Fabrication, characterisation, and finite element analysis of cold metal transfer-based wire and arc additive-manufactured aluminium alloy. Welding in the World 2021;73:331–50.

[34] Montevecchi F, Venturini G, Scippa A, Campatelli G. Finite Element Modelling of Wire-arc-additive-manufacturing Process. Procedia CIRP 2016;55:109–14. https://doi.org/10.1016/j.procir.2016.08.024.

[35] Sun J, Hensel J, Köhler M, Dilger K. Residual stress in wire and arc additively manufactured aluminum components. J Manuf Process 2021;65:97–111. https://doi.org/10.1016/j.jmapro.2021.02.021.

[36] Wu Q, Mukherjee T, De A, DebRoy T. Residual stresses in wire-arc additive manufacturing – Hierarchy of influential variables. Addit Manuf 2020;35. https://doi.org/10.1016/j.addma.2020.101355.

[37] Huang W, Wang Q, Ma N, Kitano H. Distribution characteristics of residual stresses in typical wall and pipe components built by wire arc additive manufacturing. J Manuf Process 2022;82:434–47. https://doi.org/10.1016/j.jmapro.2022.08.010.

[38] Yuan Q, Liu C, Wang W, Wang M. Residual stress distribution in a large specimen fabricated by wire-arc additive manufacturing. Science and Technology of Welding and Joining 2023;28:137–44. https://doi.org/10.1080/13621718.2022.2134963.

[39] Zhang J, Wang X, Paddea S, Zhang X. Fatigue crack propagation behaviour in wire+arc additive manufactured Ti-6Al-4V: Effects of microstructure and residual stress. Mater Des 2016;90:551–61. https://doi.org/10.1016/j.matdes.2015.10.141.

[40] Kyvelou P, Huang C, Li J, Gardner L. Residual stresses in steel I-sections strengthened by wire arc additive manufacturing. Structures 2024;60. https://doi.org/10.1016/j.istruc.2023.105828.

[41] Ge J, Ma T, Han W, Yuan T, Jin T, Fu H, et al. Thermal-induced microstructural evolution and defect distribution of wire-arc additive manufacturing 2Cr13 part: Numerical simulation and experimental characterization. Appl Therm Eng 2019;163:114335. https://doi.org/10.1016/j.applthermaleng.2019.114335.

[42] Graf M, Pradjadhiana KP, Hälsig A, Manurung YHP, Awiszus B. Numerical simulation of metallic wire arc additive manufacturing (WAAM). AIP Conf Proc 2018;1960. https://doi.org/10.1063/1.5035002.

[43] Zuo W, Chen MT, Zhao O, Su A, Liu SW, Xu F, et al. Behavior of wire arc additively manufactured 316L austenitic stainless steel single shear bolted connections. Thin-Walled Structures 2024;202:112075. https://doi.org/10.1016/j.tws.2024.112075.

[44] Zuo W, Chen M-T, Zhao O, Gardner L. Testing of Wire Arc Additively Manufactured Duplex Stainless Steel Double-Lap Shear Bolted Connections. Journal of Structural Engineering 2025;151:1–12. https://doi.org/10.1061/jsendh.steng-13999.

[45] EN ISO 6892-1. EN ISO 6892-1:2019 - Metallic materials — Tensile testing — Part 1: Method of test at room temperature 2019. https://www.iso.org/standard/78322.html (accessed October 30, 2023).

[46] Huang C, Kyvelou P, Zhang R, Ben Britton T, Gardner L. Mechanical testing and microstructural analysis of wire arc additively manufactured steels. Mater Des 2022;216:110544. https://doi.org/10.1016/j.matdes.2022.110544.

[47] EN ISO 10025-3. EN ISO 10025-3:2019 Hot rolled products of structural steels Technical delivery conditions for normalized/normalized rolled weldable fine grain structural steels 2019. https://www.en-standard.eu/bs-en-10025-3-2019-hot-rolled-products-of-structural-steels-technical-delivery-conditions-for-normalized-normalized-rolled-weldable-fine-grain-structural-steels/ (accessed October 30, 2023).

[48] Zuo W, Chen MT, Zhao O, Su A, Liu SW, Yun X, et al. Structural performance of wire arc additively manufactured duplex stainless steel single-lap shear bolted connections. Eng Struct 2024;319:118706. https://doi.org/10.1016/j.engstruct.2024.118706.

[49] Zuo W, Chen MT, Liu SW, Yun X, Zhao O, Huang Y, et al. Experimental investigation on double-lap shear behavior of 3D printed austenitic stainless steel bolted connections. Eng Struct 2024;317:118501. https://doi.org/10.1016/j.engstruct.2024.118501.

[50] Chen MT, Chen Y, Zuo W, Yun X, Zhao O, Liu SW, et al. Experimental investigation on the tensile behavior of wire arc additively manufactured duplex stainless steel plates. Eng Struct 2024;321:118764. https://doi.org/10.1016/j.engstruct.2024.118764.

[51] Chen MT, Zhang T, Gong Z, Zuo W, Wang Z, Zong L, et al. Mechanical properties and microstructure characteristics of wire arc additively manufactured high-strength steels. Eng Struct 2024;300:117092. https://doi.org/10.1016/j.engstruct.2023.117092.

[52] Montevecchi F, Venturini G, Grossi N, Scippa A, Campatelli G. Idle time selection for wire-arc additive manufacturing: A finite element-based technique. Addit Manuf 2018;21:479–86. https://doi.org/10.1016/j.addma.2018.01.007.

[53] Saunders N, Guo Z, Li X, Miodownik AP, Schillé JP. Using JMatPro to model materials properties and behavior. Jom 2003;55:60–5. https://doi.org/10.1007/s11837-003-0013-2.

[54] Farias FWC, da Cruz Payão Filho J, Moraes e Oliveira VHP. Prediction of the interpass temperature of a wire arc additive manufactured wall: FEM simulations and artificial neural network. Addit Manuf 2021;48. https://doi.org/10.1016/j.addma.2021.102387.

[55] Deng D, Murakawa H, Liang W. Numerical simulation of welding distortion in large structures. Comput Methods Appl Mech Eng 2007;196:4613–27. https://doi.org/10.1016/j.cma.2007.05.023.

[56] Goldak JA, Akhlaghi M. Computational welding mechanics. Springer; 2005.

[57] Radaj D. Heat effects of welding: temperature field, residual stress, distortion. Springer Science & Business Media; 2012.

[58] Lindgren L-E. Computational welding mechanics. Elsevier; 2014.

[59] Yang J, Kyvelou P, Wadee MA, Gardner L. Simulation and prediction of residual stresses in WAAM-strengthened I-sections. Structures 2024;69:107248. https://doi.org/10.1016/j.istruc.2024.107248.

[60] Geng H, Li J, Xiong J, Lin X. Optimisation of interpass temperature and heat input for wire and arc additive manufacturing 5A06 aluminium alloy. Science and Technology of Welding and Joining 2017;22:472–83. https://doi.org/10.1080/13621718.2016.1259031.

[61] Tan C, Li Q, Yao X, Chen L, Su J, Ng FL, et al. Machine Learning Customized Novel Material for Energy-Efficient 4D Printing. Advanced Science 2023. https://doi.org/10.1002/advs.202206607.

[62] Sun J, Hensel J, Köhler M, Dilger K. Residual stress in wire and arc additively manufactured aluminum components. J Manuf Process 2021;65:97–111. https://doi.org/10.1016/j.jmapro.2021.02.021.

[63] Fu G, Lourenco MI, Duan M, Estefen SF. Effect of boundary conditions on residual stress and distortion in T-joint welds. J Constr Steel Res 2014;102:121–35. https://doi.org/10.1016/j.jcsr.2014.07.008.

[64] Bikas H, Stavropoulos P, Chryssolouris G. Additive manufacturing methods and modeling approaches: A critical review. International Journal of Advanced Manufacturing Technology 2016;83:389–405. https://doi.org/10.1007/s00170-015-7576-2.

[65] Shinoda J, Kazanci OB, Tanabe S ichi, Olesen BW. A review of the surface heat transfer coefficients of radiant heating and cooling systems. Build Environ 2019;159. https://doi.org/10.1016/j.buildenv.2019.05.034.

[66] Martyushev SG, Miroshnichenko I V., Sheremet MA. Influence of the geometric parameter on the regimes of natural convection and thermal surface radiation in a closed parallelepiped. Journal of Engineering Physics and Thermophysics 2015;88:1522–9. https://doi.org/10.1007/S10891-015-1338-8.

[67] Ponomareva T, Ponomarev M, Kisarev A, Ivanov M. Wire arc additive manufacturing of Al-Mg alloy with the addition of scandium and zirconium. Materials 2021;14. https://doi.org/10.3390/ma14133665.

[68] Hejripour F, Binesh F, Hebel M, Aidun DK. Thermal modeling and characterization of wire arc additive manufactured duplex stainless steel. J Mater Process Technol 2019;272:58–71. https://doi.org/10.1016/j.jmatprotec.2019.05.003.

[69] Brown K, Morrow C, Durbin S, Baca A. Guideline for bolted joint design and analysis: version 1.0. 2008.

[70] Chen MT, Zuo W, Chen Y, Zhao O, Cheng B, Zhao J. Parametric topology optimization design and analysis of additively manufactured joints in spatial grid structures. Eng Struct 2024;300:117123. https://doi.org/10.1016/j.engstruct.2023.117123.

[71] Zuo W, Chen MT, Chen Y, Zhao O, Cheng B, Zhao J. Additive manufacturing oriented parametric topology optimization design and numerical analysis of steel joints in gridshell structures. Thin-Walled Structures 2023;188:110817. https://doi.org/10.1016/j.tws.2023.110817.